BIAXIALLY TEXTURED $YBa_2Cu_3O_{7-\delta}$ CONDUCTORS ON RABiTS™ WITH CRITICAL CURRENT DENSITIES OF 2–3 MA/cm²

The strong dependence of critical current density (J_c) on basal-plane grain boundary misorientation angle is well documented for most families of high transition temperature superconductors (HTS).[1–5] Furthermore, most applications of HTS, such as transformers, generators, and motors, require high-current-carrying capability in magnetic fields in excess of 0.1 T. The highly anisotropic, Bi-based superconductors are intrinsically limited in this regard in liquid nitrogen (65–77 K) because of thermally activated flux flow. Hence, a biaxially textured YBCO conductor is needed to meet application requirements of a high J_c in modest magnetic fields at liquid nitrogen temperatures.

Several methods have been proposed to produce biaxially textured conductors. One approach is to use ion-beam-assisted deposition (IBAD) to grow biaxially textured yttria-stabilized zirconia (YSZ) buffer layers on Ni-based superalloys.[6–8] This approach has produced a J_c of 1×10^6 A/cm² (77 K, 0 T) with a 1-μm thick YBCO film. Another method is to use industrially scalable, thermomechanical processes to impart a strong biaxial texture to the metal substrate itself, followed by epitaxial deposition of buffer layers and superconductor. This method, called RABiTS™ (for rolling-assisted biaxially textured substrates), has been recently demonstrated to produce J_cs of 3×10^5 A/cm² (77 K, 0 T) using a substrate configuration of YSZ (0.2 μm)/CeO2 (0.9 μm)/Pd (0.02 μm)/Ni (125 μm).[9] A different substrate configuration of YSZ (0.2μm)/CeO2 (0.9 μm)/Ni (125 μm) resulted in a J_c of 7.3×10^5 A/cm² (77 K, 0 T).[10] In both of these cases, all the oxide layers, as well as the superconductor, were deposited using pulsed laser deposition (PLD). Oxide buffer layers on textured Ni have also been deposited using electron beam (e-beam) evaporation[11] and sputtering.[12] J_cs of 6–8×10^5 A/cm² at 77 K, 0 T have been obtained on these substrates for 1-μm YBCO films grown by PLD. It had not been clear why J_cs on these substrates have not exceeded 1×10^6 A/cm² at 77 K, 0 T, given the fact that an electron backscatter investigation[13] of hundreds of interconnected grain boundaries show that RABiTS™ with nominal in-plane orientations of 7–8° full width half maximum (FWHM) contain few adjacent grain boundaries with misorientations greater than 5°.

The importance of substrate temperature on the crystalline structure of YBCO thin films produced by PLD on YSZ had been recently pointed out by both Freyhardt et al.[14] and Low et al.[15] Accordingly, it was decided to investigate whether the substrate temperature influenced the J_c (77 K, 0 T) of YBCO films on RABiTS™. We report the achievement of J_cs approaching 3×10^6 A/cm² for thin YBCO films grown epitaxially on RABiTS™ using PLD. This improvement in J_c is thought to come about both by closely controlling the substrate temperature during deposition and by using thin buffer layers, thus eliminating some microstructural features that limit J_c, such as micro-cracks and pores.

Nickel substrates were prepared by cold-rolling nickel to a thickness of 125 μm. The nickel was then annealed at a temperature of 800°C for 2 h in a vacuum of $\sim 10^{-5}$ torr. An epitaxial layer of CeO2, ~40 nm thick, was deposited by e-beam evaporation of cerium metal onto the nickel at 650°C. Oxidation of the nickel during the heat-up phase was prevented by the presence of a reducing gas: 4% H2 in argon. The cerium oxide was formed by the in situ reaction of the cerium with water vapor present (1×10^{-5} torr) in the vacuum system during the deposition.[11,12] The deposition of CeO2 was followed by the deposition of a 500-nm-thick layer of YSZ oxide by radio-

frequency (RF) sputtering of a YSZ target while the substrate was maintained at 780ºC in a 2×10^{-2} torr background of 4% H_2 in Ar.

The RABiTS™ (nickel-plus-buffer-layers unit) was then silver-pasted to the heater in the PLD chamber (Neocera). Because observations of the heater surface with an infrared pyrometer showed significant differences in the surface temperature from that indicated by the thermocouple located in the heater block, thermocouple wires were attached directly to the nickel substrate to monitor and control the substrate temperature as accurately as possible during the depositions. A Lambda Physik EMG200 excimer laser, operating at a wavelength of 308 nm, provided 200 mJ light pulses, which, when focussed by a lens with a focal length of 350 mm, produced a 3 J/cm^2 fluence at the YBCO target. During the deposition, the oxygen pressure was maintained at 200 mtorr at a flow rate of 15 scc/min. To minimize both the rate of cone formation and changes in stoichiometry on the surface of the YBCO during laser irradiation, the YBCO target was rotated at 21 revolutions per minute.

Three substrate temperatures, 740ºC, 765ºC, and 785ºC, were used to find the optimum for the given conditions. These temperature conditions will be hereafter referred to as treatment A, treatment B, and treatment C, respectively. Temperature control was provided by a Eurotherm model 808 programmable temperature controller. The YBCO growth rate was ~0.04 nm/s. After the deposition was complete, the sample was cooled at a rate of 5ºC/min in 300 torr of oxygen to 500ºC to ensure full oxygen uptake by the YBCO, at which point additional oxygen was added to bring the pressure to 500 torr. This temperature and pressure was maintained for 4 h. Finally, the substrate was cooled to room temperature at a rate of 1ºC/min. Four silver electrical contacts were then sputtered onto the YBCO surface.

Comparison of thermocouple substrate temperature readings with the heater-block temperature readings confirmed the IR pyrometer observation that the heater surface was much hotter. Moreover, it was observed that the substrate temperature would fall by as much as 25ºC during the course of the deposition if the temperature controller maintained a constant heater-block temperature. Although the authors were unaware of the fact at the time, this is in concordance with the Kiss et al.[16] IR observation of substrate temperature changes of PLD of YBCO on MgO. For the present case, the Eurotherm controller was able to keep the temperature stable to within 1ºC when controlling for substrate temperature. An alternative method for maintaining tight control of the substrate temperature has been reported by Freyhardt et al.[14] who keep the substrates within a blackbody-like enclosure, exposing the substrates only when the laser fires.

XRD θ-2θ scans (Philips) for all three cases show strong 00l orientation for the YBCO. In addition, ϕ scans, as shown in Fig. 1.1, show cube-on-cube structure with an 8.2º FWHM in-plane orientation and a 5.6º FWHM for c-axis orientation. Electrical transport measurements were performed using 4-probe techniques. Resistivity measurements employed a constant current of 40 mA. The J_c measurements were made in a different 4-probe device, with the capability of applying magnetic fields at various orientations. A 1µV/cm criterion was used for transport J_c. Film thicknesses were measured by etching the YBCO and performing profilometer measurements. X-ray energy-dispersive spectroscopy (EDS) was used to ensure that all the YBCO had been etched away from the YSZ layer. Thickness measurements were also confirmed using Rutherford Backscattering Spectroscopy (RBS). The measured critical temperatures (T_c) showed a nearly linear relationship with deposition temperature over the narrow deposition temperature range, with values of 85.8 K for treatment A, 86.6 K for treatment B, and 87.6 K for treatment C. The transition widths were all less than 2 K.
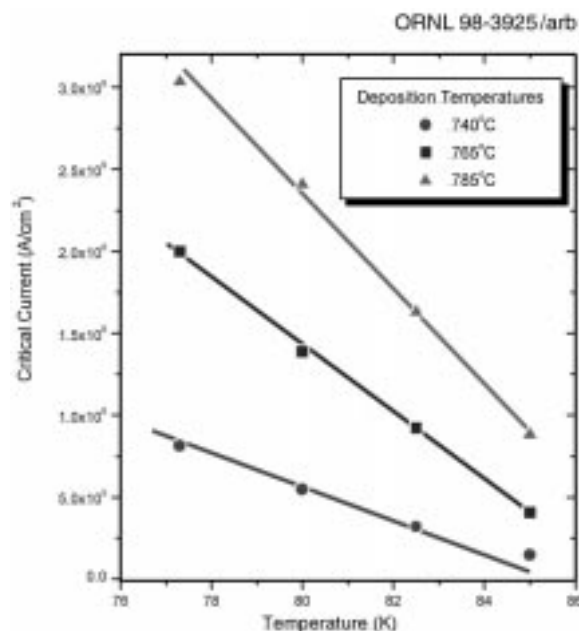
Zero-field measurements at 77 K revealed an increase in I_c with increasing deposition temperature as shown in Fig. 1.2. However, measurement of J_c for the best sample,
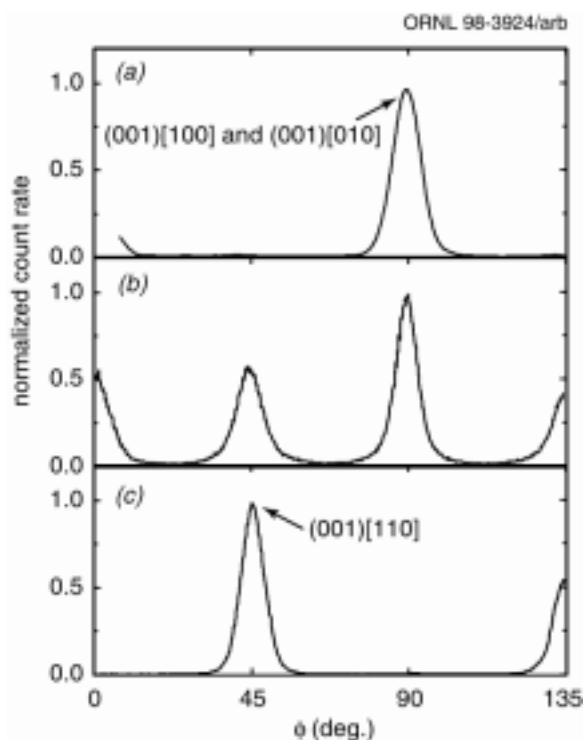
Fig. 1.1. XRD azimuthal (φ) scans indicating the in-plane alignment of YBCO/YSZ/CeO$_2$ films on thermo-mechanically textured Ni substrate. (*a*) (102) + (012) planes of treatment B, illustrating (001)[100] and (001)[010] alignment. (*b*) (103) + (013) planes of treatment A, illustrating mixed alignment. (*c*) (103) + (013) planes of treatment C, illustrating (001)[110] alignment.

Fig. 1.2. Variation in zero-field I_c as a function of temperature for the three deposition temperatures.

treatment C, was limited by current-contact heating. To estimate the value at 77 K, an extrapolation of the data from three higher temperatures was made. The resulting linear fit (R^2 = 0.9999) gave a J_c (77 K) of 3.2×10^6 A/cm^2. The sample deposited at 765ºC had a slightly lower J_c at 77 K (directly measured) of 2.4×10^6 A/cm^2, whereas the 740ºC sample had a much lower J_c at 77 K of 0.81×10^6 A/cm^2. Film thicknesses ranged from 206 nm to 250 nm, with all the substrates being 3 mm wide.

For the best film, J_c measurements were made at 77 K as a function of applied magnetic field, for $H\|c$. The field dependence was similar to that for epitaxial films on single-crystal substrates and demonstrates strongly linked behavior. With each of the three samples, a control sample of SrTiO$_3$ was placed in the PLD chamber alongside the RABiTS™. Figure 1.3 shows J_c vs H for the YBCO film on the SrTiO$_3$ crystal made together with the YBCO film on the RABiTS™ sample C. The zero-field J_c at 77 K for the film on SrTiO$_3$ was measured to be $\sim 3 \times 10^6$ A/cm^2.

Scanning electron microscope (SEM) images of the best film, shown in Fig. 1.4, display a very dense YBCO morphology, with very little structure evident. No evidence of any [100]/[010] micro-cracking is observed in the YBCO layer. This is in contrast to what was typically seen in buffer layers with a 0.9-µm-thick CeO$_2$ layer and a 0.2-µm-thick YSZ layer as summarized in a recent overview paper.[17]

In conclusion, PLD of YBCO on buffer layers deposited by industrially scalable e-beam evaporation and RF sputtering methods onto nickel resulted in superconducting I_cs and flux
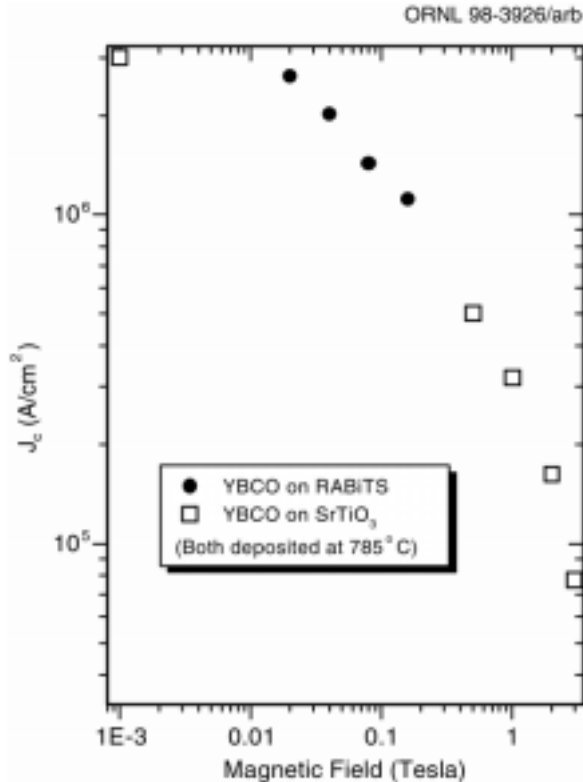
ORNL 98-3926/arb

Fig. 1.3. J_c **vs** H **for sample C and for a YBCO film grown epitaxially on SrTiO$_3$ alongside the RABiTS™.**
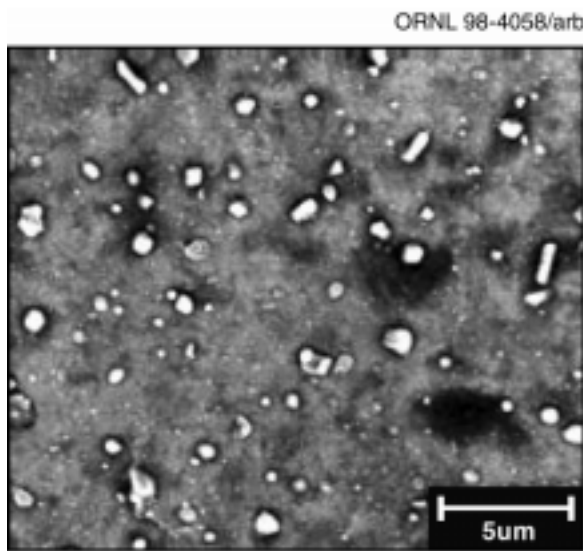
ORNL 98-4058/arb

Fig. 1.4. SEM photograph of the YBCO layer showing the dense surface morphology.

pinning behavior comparable with the best obtained for YBCO on single-crystal substrates. It is possible that the achievement of the higher J_cs of YBCO on RABiTS™ may be attributed to the closer temperature control of the substrate temperature and the use of thinner buffer layers.

References

1. D. Dimos et al., *Phys. Rev. Lett.* **61,** 219 (1988).

2. D. Dimos, P. Chaudhari, and J. Mannhart, *Phys. Rev. B* **41,** 4038 (1990).

3. A. H. Cardona et al., *Appl. Phys. Lett.* **62,** 411 (1993).

4. M. Kawasaki et al., *Appl. Phys. Lett.* **62,** 417 (1993).

5. T. Nabatame et al., *Appl. Phys. Lett.* **65,** 776 (1994).

6. Y. Iijima et al., *Appl. Phys. Lett.* **60,** 769 (1992).

7. R. P. Reade et al., *Appl. Phys. Lett.*, **61,** 2231 (1992).

8. X. D. Wu et al., *Appl. Phys. Lett.* **65,** 1961 (1994); X. D. Wu et al., *Appl. Phys. Lett.* **67,** 2397 (1995).

9. A. Goyal et al., *Appl. Phys. Lett.* **69,** 1795 (1996).

10. D. P. Norton et al., *Science* **274,** 755 (1996).

11. M. Paranthaman et al., *Physica* C **275,** 266 (1997).

12. Qing He et al., *Physica* C **275,** 155 (1997).

13. A. Goyal et al., To be published in the *J. Mater. Res.* 10th Anniversary Special Issue (Nov. 1997).

14. H. C. Freyhardt et al., *Proceedings of the Applied Superconductivity Conference*, Pittsburgh (August 25–30, 1996).

15. B. L. Low et al., *Supercond. Sci. Technol.*, **10,** 41–46 (1997).

16. T. Kiss et al., *IEICE Trans. Elec.*, **E79-C,** 1269–1273 (1996).

17. A. Goyal et al., To be published in Special Issue of *Applied Superconductivity* on YBCO Conductor Development (1997).

PULSED-LASER DEPOSITION OF OXIDE BUFFER LAYERS AND YBCO ON ROLLED-TEXTURED (001) Ni

Reproducibility of J_c in YBCO/Buffer Layers/Ni Structures

Initial results have identified the YBCO/buffer layer oxides/rolled-textured (001) Ni architecture as a viable approach to producing a deposited HTS conductor. Efforts have continued in understanding and improving the properties of these multilayer structures deposited by a number of techniques, including PLD. Figure 1.5 shows the value of J_c for a number of YBCO films grown on RABiTS™ in which both the buffer layers and YBCO were deposited using PLD. Relatively thick (> 0.5 µm) YBCO films have been obtained on rolled textured Ni, with J_c as high as 1.4 MA/cm². However, the sample-to-sample variation is relatively high. Much of the scatter observed in the plot is the result of samples that were synthesized under conditions that were not optimal. Nevertheless, the scatter in J_c reflects
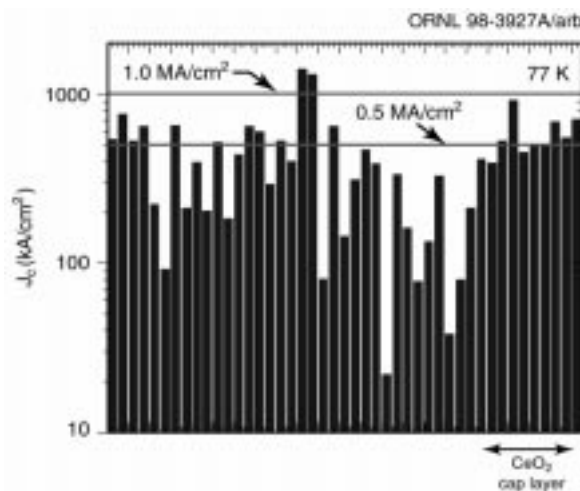

Fig. 1.5. Plot of J_c for various YBCO/buffer layers/Ni samples. YBCO film thickness is > 0.5 µm for all samples considered.

the need to improve the reproducibility in the film properties.

One important factor to consider for the YBCO/YSZ/CeO$_2$/Ni architecture involves the in-plane orientation of the YBCO films on the YSZ layers. Because of a large lattice mismatch, two distinct in-plane orientations of YBCO on (100) YSZ are often observed as illustrated in the XRD ϕ-scan in Fig. 1.6. The presence of two in-plane orientations leads to 45° grain boundaries and a subsequent reduction in J_c. Previous work has shown that various oxide buffer layers, including CeO$_2$, can significantly suppress one of these orientations. Growing YBCO/CeO$_2$/YSZ/CeO$_2$/Ni structures with a thin (~ 200Å) CeO$_2$ cap layer on the YSZ improves the reproducibility of J_c. As seen in Fig. 1.5, YBCO films can be routinely obtained on RABiTS™ with J_c (77 K) > 0.5 MA/cm² and
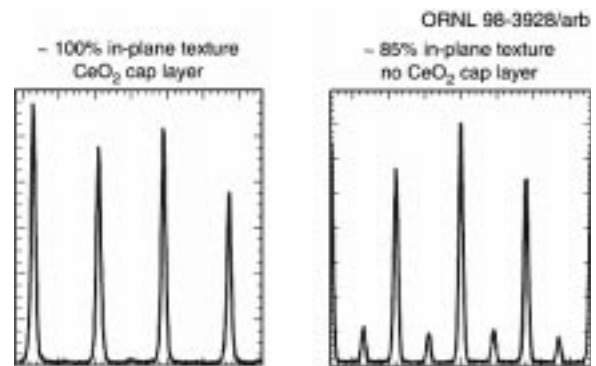

Fig. 1.6. XRD ϕ-scans for YBCO films deposited on RABiTS™ with and without CeO$_2$ cap layers.

only one in-plane orientation when CeO$_2$ is utilized to eliminate secondary in-plane orientations. Efforts continue to understand other factors, such as strain or microstructure, that influence J_c for YBCO films on RABiTS™.

Transmission Electron Microscopy of YBCO/Buffer Layers/Ni Structures

A fundamental understanding of the epitaxial oxide/metal multilayer structure is

crucial in efforts to effectively characterize and further improve the performance of RABiTS™-based HTS conductors. Microstructural analysis using cross-section transmission electron microscopy (TEM) has been performed on YBCO/buffer layer/Ni structures. Figure 1.7 shows results from a cross-section TEM image of a YBCO/YSZ/CeO$_2$/Ni structure. This cross section reveals each of the oxide layers and includes a grain boundary that originates from the Ni substrate. There are several features of interest in this micrograph. First, significant oxidation of the nickel substrate is evident at the Ni/CeO$_2$ interface. It is assumed that this NiO layer forms after the nucleation of (100) CeO$_2$ occurs on the (100) Ni surface. The formation of a NiO layer at the metal/oxide layer interface should have significant influence on the mechanical and adhesive properties of the film because of stresses related to the volume change with the oxidation of Ni at the buried interface. From the image, we note that the morphology of the thermally etched grain boundary is reproduced in all of the oxide layers. We also
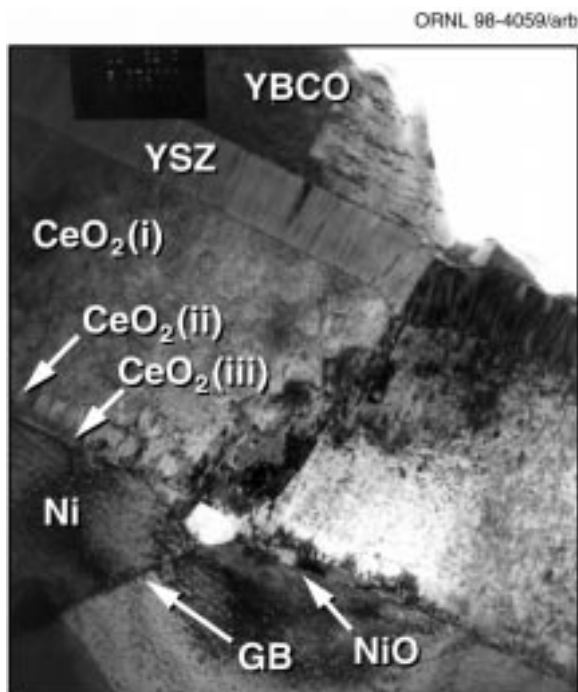
observe that the microstructure of the CeO$_2$ is dependent on film growth conditions, with distinct microstructures observed for CeO$_2$ deposited in a vacuum, hydrogen, or oxygen background. The YSZ layer also displays a distinctive columnar microstructure. Future efforts will focus on understanding how specific oxide microstructures affect the mechanical properties of these multilayer structures.

Microstructural characterization of YBCO on RABiTS™ using plan-view Z-contrast scanning transmission electron microscopy (Z-STEM) provides insight regarding the atomic structure of the YBCO grain boundaries for films deposited on these substrates. Figure 1.8 shows an atomic resolution Z-STEM image of a typical YBCO low-angle grain boundary that is commonly observed in *c*-axis oriented YBCO films deposited on rolled-textured (001) Ni tape. These low-angle grain boundaries in epitaxial YBCO film on RABiTS™ originate from the grain structure in the biaxially textured (001) Ni tape. As seen in the figure, the atomic structure of the grain boundary closely resembles that observed for YBCO films on SrTiO$_3$ bicrystals, consisting of a "clean" boundary with a regular array of dislocation cores. From the micrograph, there is no evidence for impurity phases, NiO,

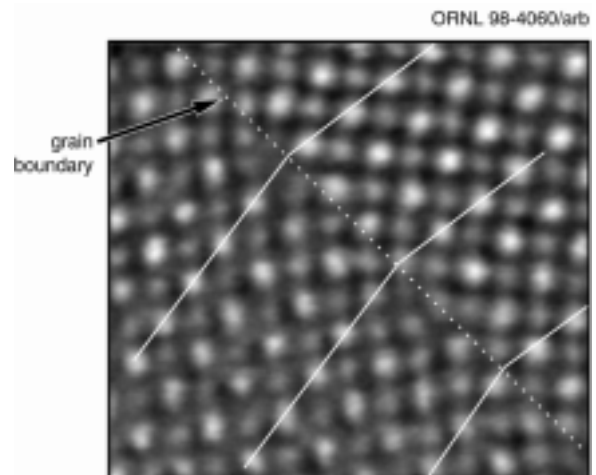**Fig. 1.7. Cross-section TEM image of YBCO/YSZ/CeO/Ni structure.**

Fig. 1.8. Plan-view Z-contrast scanning electron microscopy image of a YBCO grain boundary for a *c*-axis oriented film deposited on rolled-textured (001) Ni.

or misoriented YBCO grains at the boundary. This is consistent with the relatively high I_cs that are observed for YBCO/buffer layers/(001) biaxially textured Ni structures.

Bend Strain Tolerance of J_c

An important aspect for any HTS wire technology involves the degree to which the conductor can be bent without damaging the conductor. To address this issue, bend strain tolerance mesurements have been performed on RABiTS™. The bend strain tolerance for two of YBCO/buffer layers/Ni tapes measuring both tensile and compressive strain is shown in Fig. 1.9. For both of these samples, the buffer layers and YBCO were deposited using PLD. The samples were placed in strain by deforming the tapes over a selected radius of curvature at room temperature. The strain is then removed (sample curvature is removed) for J_c measurement in liquid nitrogen. Each data point

in the plots represents bending, straightening, and thermal cycling. The initial J_c (77 K) for each sample was greater than 0.5 MA/cm^2. For compressive strain, significant degradation of J_c was not observed until the bend strain exceeded 0.7%, at which point failure was catastrophic. SEM images of this sample after strain tolerance measurements indicate the presence of long cracks that extend a significant fraction of the sample width. The observation of long cracks in the YBCO film is consistent with the catastrophic failure that was observed in the behavior of J_c. For the case of tensile strain, a significant decrease in J_c with applied strain began at ~ 0.3 %. In contrast to the behavior observed for compressive strain, failure of the sample with tensile strain was more gradual, with complete failure ($J_c = 0$) observed for a strain of ~ 0.5%. The SEM micrograph for this sample shows an array of short fracture lines with the density of cracks higher for the tensile strain than for the sample placed in

ORNL 98-3929/arb
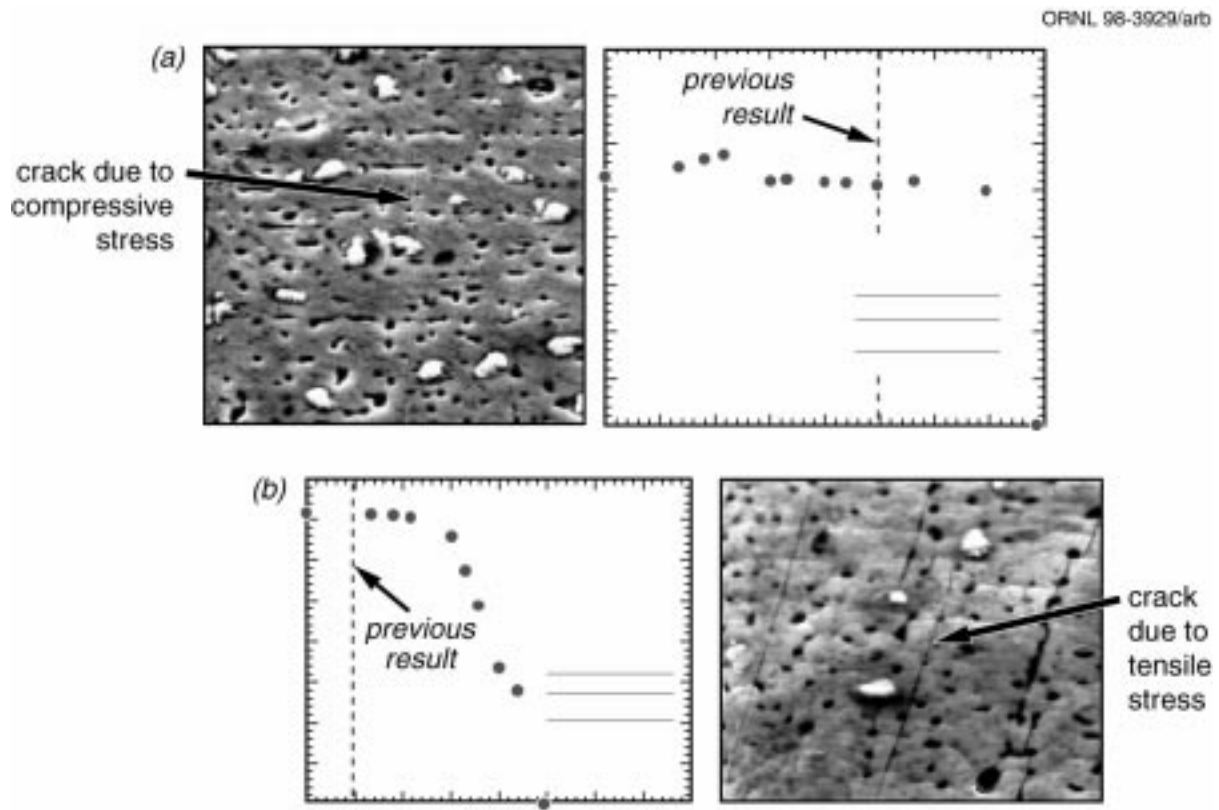
Fig. 1.9. Bend strain tolerance for two YBCO/buffer layers/Ni tapes measuring (*a*) compressive and (*b*) tensile stress.

compression. The appearance of short cracks is consistent with a gradual failure of the film for tensile strain. The strain tolerance for these samples is better than previous results in which the total oxide layer thickness was significantly larger. Future efforts will continue to focus on the effects of specific multilayer oxide architectures on the strain tolerance.

Efforts To Engineer High J_e Conductors Using Thin Rolled-Textured Ni

The use of thinner (001) Ni tapes holds the promise of achieving high engineering critical current densities (J_e) with 1–2-µm-thick YBCO films. Previous results have shown that Ni could be rolled-textured to a thickness of ~25 µm with in-plane and out-of-plane texture similar to that obtained for 125-µm-thick Ni tapes. Initial efforts have focused on the epitaxial growth of the YBCO/YSZ/CeO$_2$ oxide architecture on 25-µm-thick Ni tapes using PLD. Figure 1.10 shows the XRD rocking curves for the buffer and YBCO layers. Four-circle XRD shows that the oxide layers are epitaxial and in-plane aligned with respect to the Ni substrate. The best result achieved to date with 25 µm-thick Ni substrates is J_c (77 K) ~ 200 kA/cm^2.

Significantly higher values for J_c are anticipated as superior procedures for handling these relatively thin metal tapes are developed. Future efforts will also focus on understanding the effect of substrate thickness on the conductor properties, particularly when considering the difference in thermal expansion for the oxides layers and the thin Ni tape.

Facility Development for Long-Length Conductor

Efforts to fabricate RABiTS™-based YBCO conductors with length on the order of 10–100 cm have resulted in facility development for continuous film deposition using PLD. A radiant heater capable of uniformly heating 1-cm-wide Ni tapes up to 800°C in an oxygen ambient atmosphere has been purchased from Thermionic Laboratory. This radiant heater is necessary for achieving long-length and two-sided deposition of YBCO on RABiTS™. Initial efforts will focus on 10-cm-long samples. A linear translation substrate holder capable of accommodating 10-cm-long samples has been designed and assembled. For tape length greater than 10 cm, a reel-to-reel tape drive system has been designed. This system includes vacuum
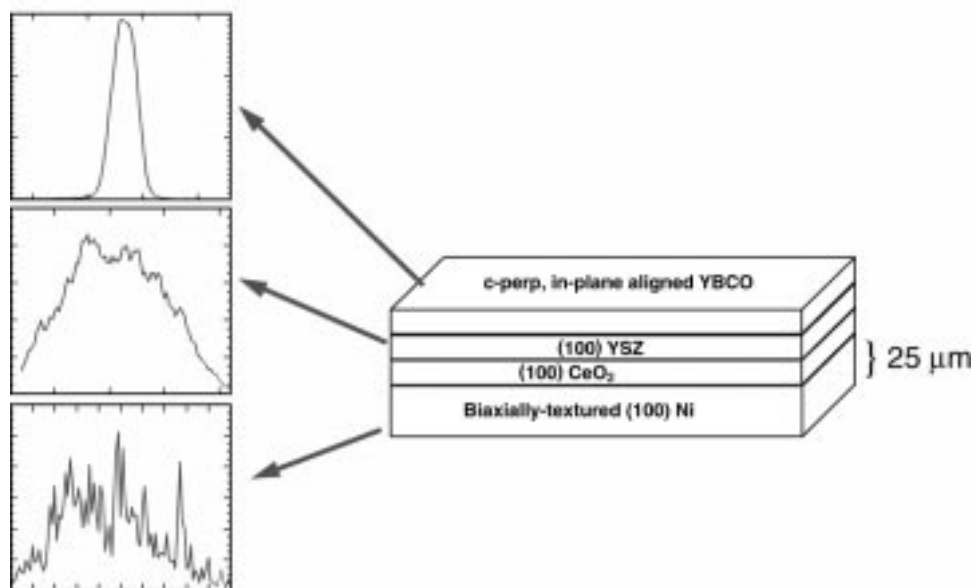
ORNL 98-3930/art

Fig. 1.10. XRD rocking curves for YBCO/YSZ/CeO$_2$ oxide architecture on a 25-µm-thick rolled-textured Ni tape.

chamber attachments with stepping motors to manipulate 1-cm-wide metal tapes of arbitrary lengths.

HIGH J_c YBCO FILMS ON BIAXIALLY TEXTURED Ni WITH OXIDE BUFFER LAYERS DEPOSITED USING ELECTRON BEAM EVAPORATION AND SPUTTERING

High J_c has been recently demonstrated for epitaxial YBCO films grown on RABiTS™.[1,2] For these first demonstrations of high J_c, both the buffer layers (CeO_2 and YSZ) and the YBCO were deposited epitaxially by in situ PLD without intermediate exposure of the substrate to atmosphere. For a practical superconducting wire technology, a more flexible fabrication scheme and an easily scalable deposition technique compared to in situ PLD is desirable. To investigate the possibility of obtaining high J_c YBCO conductors using more flexible and easily scalable ex situ methods for deposition, buffer layers have been grown on biaxially textured nickel by (a) exclusively e-beam evaporation (CeO_2 and YSZ) and (b) a combination of e-beam evaporation (CeO_2) and RF magnetron sputtering (YSZ). Although methods to deposit oxide buffer layers (CeO_2 and YSZ) exclusively by e-beam evaporation[3] and exclusively by sputtering[4] have been reported previously, no attempts to grow YBCO on these buffered substrates have been reported.

Experimental

Biaxially textured Ni substrates were formed by consecutive rolling of a polycrystalline, randomly oriented high purity (99.99%) bar to total deformations greater than 95%, followed by recrystallization.[1] Examination of (111) and (200) pole figures of an as-rolled Ni tape shows localization of intensities along the {112}<111> and the {123}<634> orientations along the β-fiber or the skeleton line, consistent with the formation of a sharp copper-type rolling texture. Controlling the surface condition of the work rolls allowed substrates with surfaces with a route mean square (rms) roughness of ~10 nm to be obtained. The substrate was then annealed in situ in a laser ablation chamber at 900°C for 2 h in 4% H_2 in Ar, resulting in the formation of a sharp {100}<100> cube texture. Typical samples showed X-ray ω- and ϕ-scans with FWHM of 6° and 7°, respectively. Grain boundary studies of the substrate using electron backscatter Kikuchi diffraction (BKD) showed that more than 95% of the boundaries had misorientations less than 5°.[5]

The deposition of CeO_2 was accomplished by e-beam evaporation and is described in detail elsewhere.[3] CeO_2 was deposited from a cerium metal melt at a substrate temperature of 625°C in 2×10^{-5} torr of 4% H_2/96% Ar. The CeO_2 was deposited at a rate of 0.1 nm/sec to a thickness of 40 nm as determined by a quartz crystal monitor. Following deposition, the substrate was cooled in 2×10^{-5} torr of 4% H_2/96% Ar to < 200°C and then was allowed to cool to room temperature in air at 1 atm.

Epitaxial YSZ was next deposited by either e-beam evaporation or RF magnetron sputtering. In both cases, the nominal composition of the starting material was 99.9% ZrO_2 with 10–15 wt % Y_2O_3. For e-beam evaporation of YSZ, a substrate of CeO_2 on Ni was cleaned in methanol and mounted in the evaporation chamber. Next it was annealed at 700°C in 1 torr of 4% H_2/96% Ar for 60 min. Deposition of YSZ was accomplished at a substrate temperature of 700°C in 2×10^{-5} torr of 4% H_2/96% Ar. The YSZ was deposited at a rate of 0.1 nm/sec to a thickness of 100 nm. Following deposition, the substrate was cooled in 2×10^{-5} torr of 4% H_2/96% Ar to < 200°C and then was allowed to cool to room temperature in air at 1 atm. For deposition of YSZ by sputtering, a substrate of CeO_2 on Ni was mounted directly in the sputtering chamber

without cleaning in methanol. It was next annealed at 780°C in 10 mtorr of 4% H_2/96% Ar for 10 min. Deposition of YSZ was accomplished at a substrate temperature of 780°C in 10 mtorr of 4% H_2/96% Ar. The YSZ was deposited at a rate of 0.1 nm/sec to a thickness of 750 nm. The sputter target was parallel to and 5 cm from the substrate surface. After deposition, the substrate was allowed to cool to < 200°C in 10 mtorr of 4% H_2/96% Ar before exposure to air at 1 atm.

YBCO was deposited on the YSZ/CeO_2/Ni substrates at 780°C in an O_2 pressure of 185 mtorr by PLD using a KrF excimer laser.[2] The substrates were cooled after deposition to 400°C at 10 C/min and then exposed to 700 mtorr of oxygen. The thickness of the YBCO films was 1 µm as determined for each substrate by profilometry.

The samples were characterized using a field emission Hitachi SA-4500 SEM, a Philips XL30 field emission microscope equipped with an electron backscatter diffraction detector, and by a Rigaku X-ray diffractometer. Electrical properties were measured using a pulsed current system reported previously.[6]

Results and Discussion

The typical microstructures of YBCO films grown by laser ablation on RABiTS™ in which the buffer layers were deposited by exclusively


ORNL 98-3782/arb
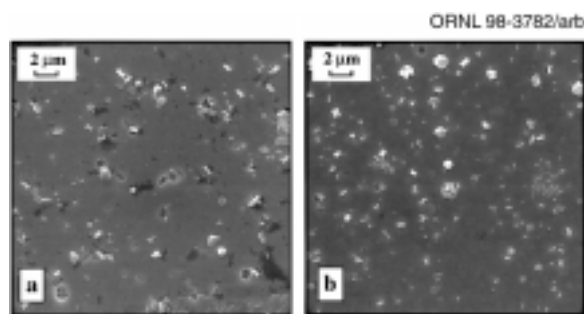
Fig. 1.11. (*a*) Scanning electron micrograph of a YBCO film deposited on exclusively e-beam buffered nickel. (*b*) Scanning e-beam micrograph of a YBCO film deposited on e-beam/sputtered buffered nickel.

e-beam evaporation or a combination of e-beam evaporation and sputtering are shown in Fig. 1.11. The micrographs were taken at a magnification of $1000 \times$ and show no evidence of any microcracks. Moreover the films appear to be very dense and continuous and to contain some surface second phase particles.

Similar to samples prepared by in situ PLD, the out-of-plane alignment of YBCO is good with a rocking curve width of ~2° FWHM. The in-plane alignment for these samples is more complex. Figure 1.12 shows the in-plane texture of YBCO film grown on the substrate in which

ORNL 98-3783/arb
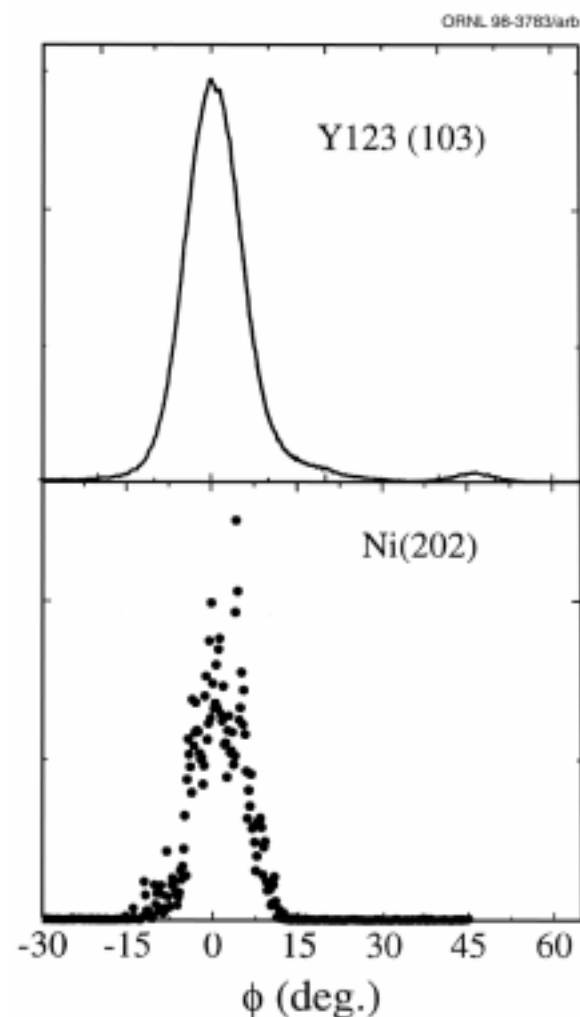
Fig.1.12. (*a*) X-ray phi scan of a YBCO film on RABiTS™ in which the buffers were put down exclusively by e-beam evaporation and (*b*) X-ray phi scan of Ni.

ORNL 98-3784/abb
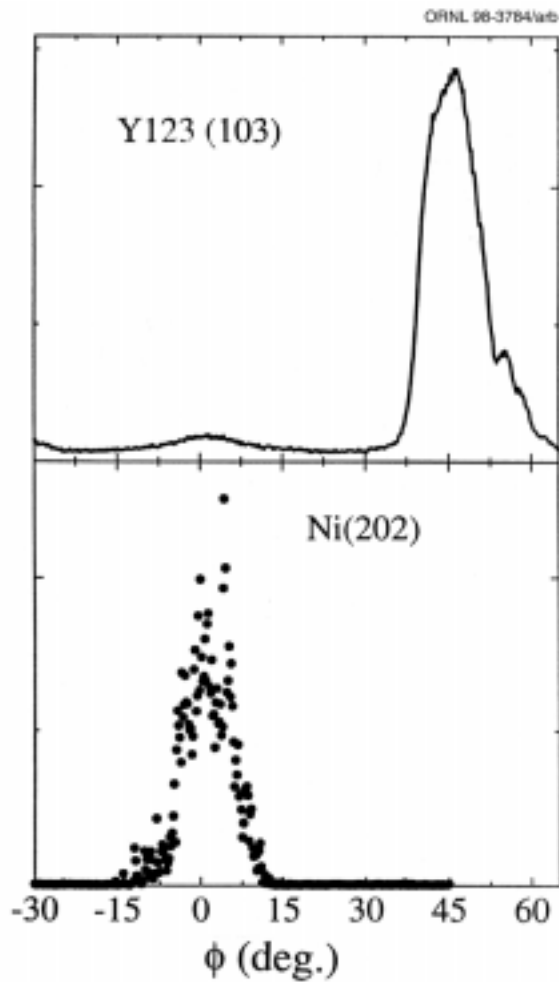
Fig.1.13. (*a*) X-ray phi scan of a YBCO film on RABiTS™ in which the buffers were put down by a combination of e-beam evaporation and sputtering and (*b*) X-ray phi scan of Ni.

the buffer layers were deposited exclusively using e-beam evaporation with respect to the texture of the underlying Ni substrate. In this case the thicknesses of the CeO_2 and YSZ layers were 10 nm and 130 nm, respectively. Figure 1.13 shows the in-plane texture of YBCO film grown on the substrate in which the buffer layers were deposited by a combination of e-beam evaporation and sputtering with respect to the texture of the underlying Ni substrate. In this case the thicknesses of the CeO_2 and YSZ layers were 10 nm and 770 nm, respectively. As in the in situ PLD samples, relative to Ni[100],

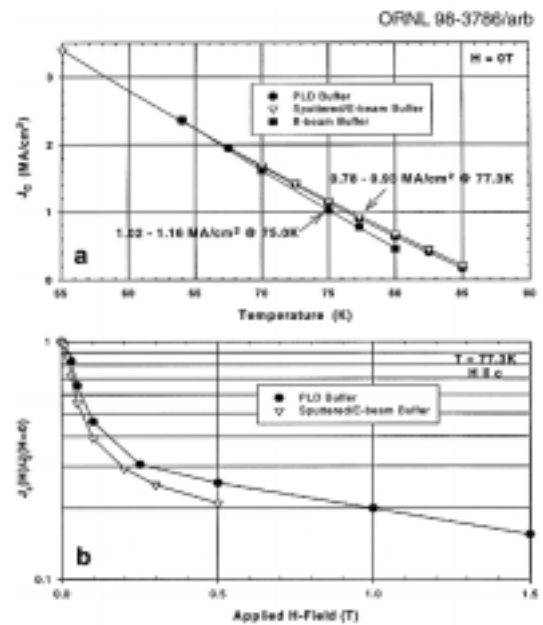CeO_2[100] and YSZ[100] are rotated $45°$ (i.e., Ni[100] ‖ CeO_2[110] ‖ YSZ[110]). The YBCO assumes two in-plane orientations relative to the YSZ, namely, the cube-on-cube orientation with YBCO([100] + [010]) ‖ YSZ[100] and the $45°$ rotated orientation with YBCO([100] + [010]) ‖ YSZ[110]. These same two-component mixtures of in-plane orientation for epitaxial YBCO were observed previously by Garrison et al.[7] and Fork et al.[8] on single crystal YSZ. They found that the distribution of orientations depends strongly on the YSZ/YBCO interfacial composition and less strongly on the temperature and pressure during YBCO deposition. In our study for the sample with buffer layers grown by exclusively e-beam, the distribution of in-plane orientations of the YBCO was 1.5% cube-on-cube and 98.5% $45°$ rotated with respect to the underlying Ni. For the sample with buffer layers grown by e-beam/sputtering, the distribution was 97% cube-on-cube and 3% $45°$ rotated with respect to the underlying Ni. This difference in preference of the YBCO epitaxial variant on YSZ may be related to different internal stresses due to different thicknesses of YSZ layers.

Figure 1.14 (top) shows an orientation image micrograph of the Ni substrate. The micrograph was obtained using BKD. Gray level shading on the micrograph is a reflection of the pattern quality or intensity of the Kikuchi bands observed at each point. Grain boundaries give rise to multiple diffraction patterns and hence have a poor pattern. Similarly, poor patterns are observed from any other crystallographic defect or strained region. BKD patterns were obtained on a hexagonal grid with a spacing of 0.6 µm. Indexing of the pattern at each location gave a unique measure of the orientation at that point. A hypothetical hexagonal lattice with a grain size of 0.6 µm was superimposed at each point from which a pattern was obtained. Grain boundary misorientations were then calculated for all the resulting boundaries using standard techniques. The micrograph was then regenerated to reveal high angle boundaries, and the only high angle boundaries found were those

ORNL 98-3785/arb
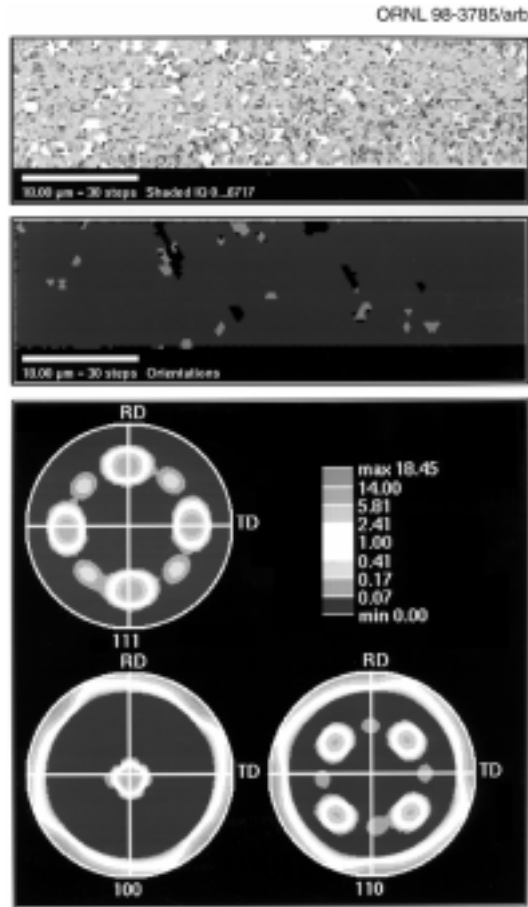
Fig. 1.14. (*top*) In-plane orientation map of a YBCO film deposited on e-beam/sputtered buffered nickel. (*middle*) The dark and light areas are regions of YBCO with cube-on-cube orientation and 45° rotated orientation, respectively. (*bottom*) Corresponding (111), (100), and (110) pole figures.

ORNL 98-3786/arb

Fig. 1.15. Temperature (*a*) and magnetic field dependence (*b*) of J_c for YBCO films on buffer layers prepared by PLD, sputtering/e-beam, and e-beam on biaxially textured nickel.

surrounding 45° rotated YBCO grains. In Fig. 1.14 (middle), dark and light areas are regions of YBCO with cube-on-cube orientation and 45° rotated orientation, respectively. Corresponding (111), (100), and (110) pole figures are shown in Fig. 1.14 (bottom). The dark grains in Fig. 1.14 (middle) correspond to the 45° rotated cube location in the pole figure. Approximately 3 vol % of YBCO is rotated 45°. Clearly, the supercurrent will not be disrupted significantly by the presence of this second orientation.

With a voltage criterion of 1 µV/cm, transport J_c was measured for the e-beam and the sputtered/e-beam samples in a pulsed current system. Figure 1.15(*a*) shows the temperature dependence of J_c for the two samples along with that for a sample with buffer layers and YBCO prepared by in situ PLD. For the in situ all-PLD sample, the distribution of in-plane orientations of the YBCO was 10% cube-on-cube and 90% 45° rotated. All three samples show high J_c at 77.3 K (0.78–0.93 MA/cm^2) and a similar temperature dependence of J_c. The dependence of J_c on magnetic field is also similar for the sputtered/e-beam sample and the all-PLD sample [see Fig. 1.15(*b*)]. The e-beam sample was damaged during the measurement of J_c as a function of the temperature and could not be used during the measurement of J_c as a function of field.

These results are the first demonstration of high J_c for epitaxial YBCO films on biaxially textured nickel with buffer layers deposited by

ex situ non-PLD methods. They suggest the feasibility of more flexible and practical methods of fabrication of coated YBCO superconducting wire of long length.

Summary

High J_c YBCO films were prepared on RABiTS™ composed of CeO_2/YSZ/Ni in which the oxide layers were deposited ex situ using either e-beam or sputtering. This result is significant for several reasons. First, it demonstrates that ex situ deposition of YBCO films can be successfully performed on buffered Ni that has been exposed to air. This is important from a manufacturing point of view. Second, it demonstrates that crack-free, epitaxial, oxide buffer layers can be deposited on Ni using the scalable techniques of e-beam evaporation and sputtering.

References

1. A. Goyal et al., "High Critical Density Superconducting Tapes by Epitaxial Deposition of $YBa_2Cu_3O_x$ Thick Films on Biaxially Textured Substrates," *Appl. Phys. Lett.* **69** (12), 1795–97 (Sept. 16, 1996); A. Goyal et al., patent pending.

2. D. P. Norton et al., "Epitaxial $YBa_2Cu_3O_7$ on Biaxially Textured Nickel (001): An Approach to Superconducting Tapes with High Critical Current Density," *Science,* **274**, 755–757 (Nov. 1, 1996).

3. M. Paranthaman et al., *Physica C,* **275**, 266 (1997).

4. Q. He et al., *Physica C,* **275**, 155 (1997).

5. A. Goyal et al., "Conductors with Controlled Grain Boundaries: An Approach to the Next Generation, HighTemperature Superconducting Wire," *J. Mater. Res.*, Special Issue (November 1997).

6. F. A. List, P. M. Martin, and D. M. Kroeger, *Rev. Sci. Instrum.* **67**, 3187 (1996).

7. S. M. Garrison et al., *Appl. Phys. Lett.* **58**, 2168 (1991).

8. D. K. Fork et al., *J. Mater. Res.* **7**, 1641 (1992).

GROWTH OF BIAXIALLY TEXTURED MgO BUFFER LAYERS ON ROLLED-Ni SUBSTRATES BY ELECTRON BEAM EVAPORATION

The growth of a buffer layer architecture consisting of an epitaxial laminate of MgO/Ag/Pt or MgO/Ag/Pd deposited on a biaxially textured Ni substrate is described in this report. The cube (100) texture in the Ni was produced by thermomechanical processing. Both Pd and Pt films were grown epitaxially on the rolled-Ni substrates. The Ag films were grown on Pd- and Pt-buffered Ni substrates by in situ epitaxial growth of MgO. The crystallographic orientation of the Ag and MgO was mostly (100). The MgO buffer layer developed may be useful for the growth of high current conductors.

Earlier, we developed three buffer layer architectures on textured-Ni substrates using an e-beam evaporation technique. They were Ag/Pd(Pt)/Ni, CeO_2/Ni, and YSZ/CeO_2/Ni. We also recently demonstrated a J_c of 1×10^6 A/cm^2 at 75 K and zero field on ~0.76-µm-thick $YBa_2Cu_3O_{7-y}$ (YBCO) film. This film was deposited by pulsed laser ablation on a YSZ/CeO_2/Ni substrate. All the buffer layers were deposited using the e-beam system. The total thickness of the buffer layer was 1500 Å. In this report, we discuss our successful growth of biaxially aligned MgO buffer layers on the textured-Ni substrates.

The cube (100) texture in Ni (99.99% pure) was produced by cold-rolling to over 90% deformation followed by recrystallization at 800°C. The thickness of the textured-Ni substrate used was 125 µm. The deposits were produced without any substrate polishing using an e-beam evaporation technique. The experimental details for the growth of buffer layers on rolled-Ni substrates are described in the following two sections.

Ag/Pd(Pt)/Ni Architecture

The as-rolled Ni substrates were cleaned ultrasonically with both acetone and methanol and were mounted on a substrate holder with a heater assembly in the e-beam system. After the vacuum had reached 1×10^{-6} torr at room temperature, the substrates were in situ annealed at 400 °C for 4 h. The temperature of the substrate was measured using a thermocouple. The Pd layer was then grown on the textured Ni at temperatures ranging from 100 to 500 °C. The typical deposition rate for Pd was 0.5–1.0 nm/s at a pressure of 10^{-6} torr, and the final thickness was varied from 200 nm to 1 μm. The thickness of the film was measured by a quartz crystal monitor during the deposition. The θ-2θ scan for a 400-nm-thick Pd film deposited on Ni at 500 °C showed the presence of a (100)-oriented film. A four-circle diffractometer was used to collect pole figures, to measure rocking curves (ω scan) of (002) planes of the (001)-textured film which analyze the out-of-plane alignment, and to measure φ scans of the (202) planes which analyze the in-

plane alignment of the film. Figure 1.16 shows the ω and φ scans for as-deposited Pd (400 nm thick) on Ni at 500 °C. The FWHM for Ni (002) and Pd (002) are 6.6° and 4.0°, and that of Ni (202) and Pd (202) are 13.0° and 7.1°, respectively. From Fig. 1.16, we can conclude that Pd can be grown epitaxially on Ni. Platinum films were also grown epitaxially on textured-Ni substrates using similar Pd deposition conditions. Figure 1.17 shows the ω and φ scans for as-deposited Pt (200 nm thick) on Ni at 500 °C. The FWHM for Ni (002) and Pt (002) are 10.7° and 9.3°, and that of Ni (111) and Pt (111) are 8.9° and 10.2°, respectively. This is an example where Pt was grown epitaxially on Ni.

The Ag films were then grown on both Pd-buffered and Pt-buffered Ni substrates at room temperature. The Ag films were then post-annealed at 300 °C in the system. The θ-2θ scan for a 150-nm-thick Ag film deposited on both Pd-buffered and Pt-buffered Ni showed the presence of a (100)-oriented film. Figure 1.16 also shows the ω and φ scans for 150-nm-thick post-annealed Ag films on Pd-buffered Ni

ORNL 98-3775/arb
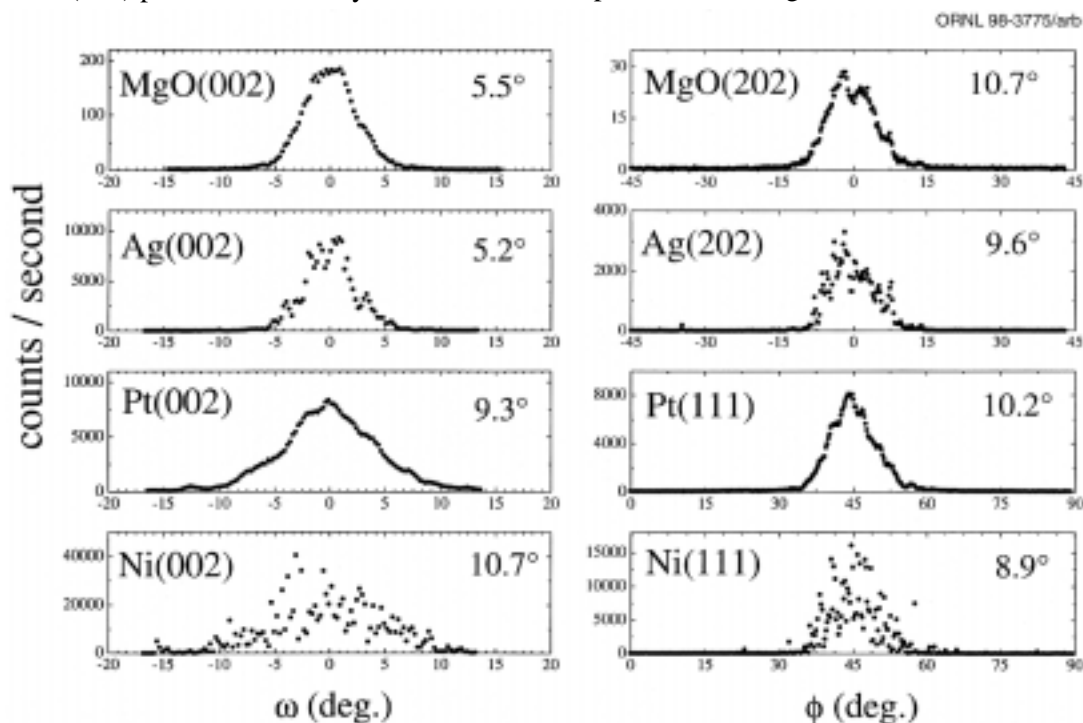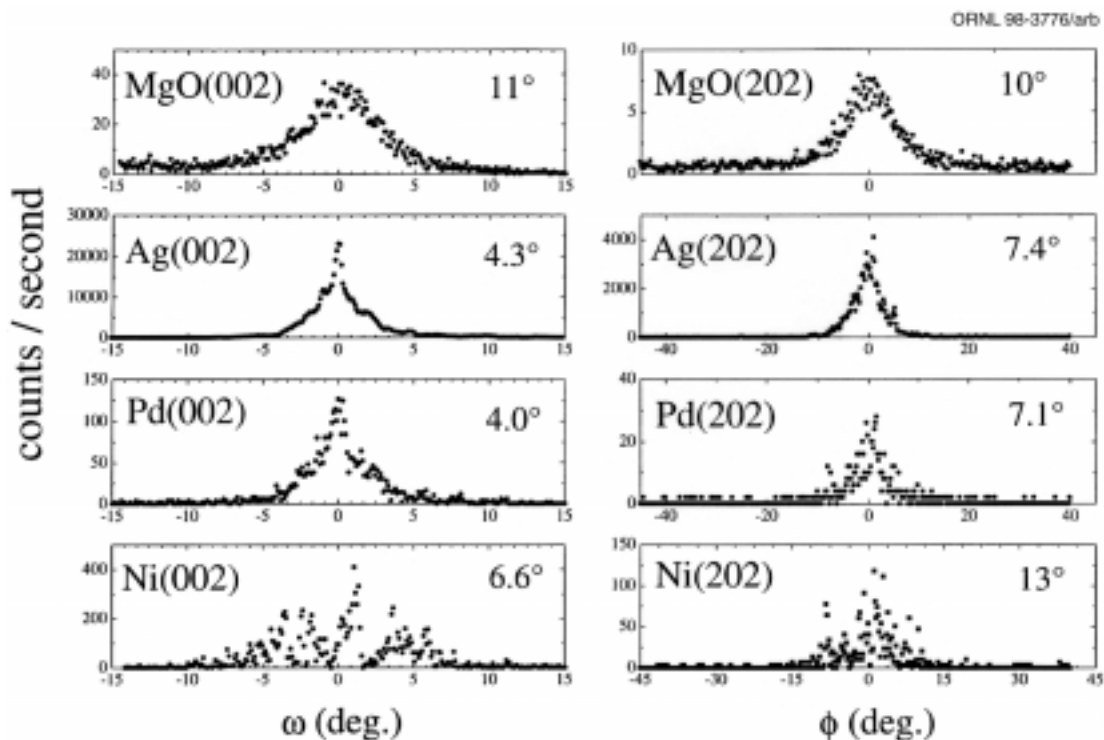

Fig. 1.16. The X-ray ω and φ scans for post-annealed 200-nm-thick MgO on Ag-Pd-buffered Ni substrates.

ORNL 98-3776/arb

Fig. 1.17. The X-ray ω and φ scans for as-deposited 200-nm-thick MgO on Ag-Pt-buffered Ni substrates.

substrates. The FWHM for Ag (002) is 4.3°, and that of Ag (202) is 7.4°, respectively. The rocking curves for Pd, Pt, and Ag are smooth because these are fine-grained films. The Ni substrate, by contrast, is coarse grained, so its rocking curves (see Figs. 1.16 and 1.17) consist of many sharp peaks corresponding to individual grains. The XRD results show that Ag, Pt, and Pd can be deposited epitaxially on Ni by the e-beam evaporation technique. Similar results were also obtained on films grown by dc sputtering.

MgO/Ag/Pd(Pt)/Ni Architecture

The MgO layers were deposited on Ag-Pt-buffered or Ag-Pd-buffered Ni substrates at room temperature using e-beam evaporation followed by in situ post-annealing up to 300°C. MgO was used as the source. The deposition rate was 0.5–1.0 nm/s at 1×10^{-5} torr vacuum with the total thickness of 200 nm. Figure 1.16

shows the ω and φ scans for 200-nm-thick post-annealed MgO films on Ag-Pd-buffered Ni substrates. The FWHM for MgO (002) is 11.0°, and that of MgO (202) is 10.0°, respectively. Figure 1.17 shows the ω and φ scans for 200-nm-thick as-deposited MgO films on Ag-Pt-buffered Ni substrates. The FWHM for MgO (002) is 5.5°, and that of MgO (202) is 10.7°, respectively. Figures 1.16 and 1.17 prove that the MgO films grown on Ag-buffered substrates are biaxially oriented. Attempts will be made to grow superconductors on these buffer layers.

DEMONSTRATION OF HIGH CURRENT YBa$_2$Cu$_3$O$_{7-y}$ COATED CONDUCTORS ON ROLLED-Ni SUBSTRATES WITH THIN BUFFER LAYERS

In the YBCO coated conductors project, the highest J_c obtained previously at ORNL was 7.3×10^5 A/cm^2 at 77 K and zero field on a

1.4-µm-thick YBCO film that has an architecture of YBCO/YSZ/CeO$_2$/Ni. Both buffer layers and YBCO superconductors were grown in situ by PLD. The total buffer layer thickness used was about 1 µm. To improve the mechanical properties of our RABiTS™ and also to increase the overall engineering current density (J_e), we investigated the effect of buffer layer thicknesses. The CeO$_2$ layer thickness was found to be critical. CeO$_2$ films with a thickness of about 100 Å were smooth, continuous, and also crack-free. In this study, we grew 1400-Å-thick YSZ films on 100-Å-thick CeO$_2$-buffered Ni substrates. The e-beam evaporation technique was used to grow both CeO$_2$ and YSZ films. The YBCO films were grown using a KrF excimer laser.

The 125-µm-thick as-rolled Ni substrates were cleaned initially with both acetone and methanol and recrystallized at 800°C to obtain the (100) cube texture. The biaxially oriented Ni substrates were then mounted on a substrate holder with a heater assembly in the e-beam system. After the vacuum in the chamber had reached 1×10^{-6} torr at room temperature, a mixture of 4% H$_2$ and 96% Ar was introduced until the pressure inside the chamber reached ~1 torr. The Ni substrates were then annealed at ~650°C for 60 min at ~1 torr. During CeO$_2$ deposition, the chamber was maintained at a pressure of 2×10^{-5} torr with a mixture of 4% H$_2$ and 96% Ar. The CeO$_2$ layers were deposited on Ni substrates at 600°C. The deposition rate for CeO$_2$ was 3–4 Å/s with an operating pressure of 10^{-5} torr, and the final thickness was 100 Å. For 100-Å-thick CeO$_2$ films, XRD results from the θ-2θ scan, and also ω and φ scans, revealed (100) texture. The YSZ layers were grown on the CeO$_2$-buffered Ni substrates at 600°C. YSZ deposition rate was 1 Å/s with the operating pressure of 2×10^{-5} torr, and the final thickness was 1400 Å. XRD results from the θ-2θ scan, and also ω and φ scans, for 1400 Å thick YSZ films also showed a strong texture. A thick (≤ 1 µm) YBCO film was then deposited on the YSZ using PLD at 780°C. The oxygen pressure was 185 mtorr. After deposition, the films were cooled at 10°C/min, and the oxygen pressure was increased to 700 torr at 400°C. The θ-2θ scan on the YBCO film showed the presence of a *c*-axis aligned film. The thickness of the YBCO film was found to be 0.76 µm using a profilometer scan. These films were 0.3 cm wide and 1 cm long. The φ scan for 0.76-µm-thick YBCO film on the RABiTS™ is shown in Fig. 1.18. It shows the
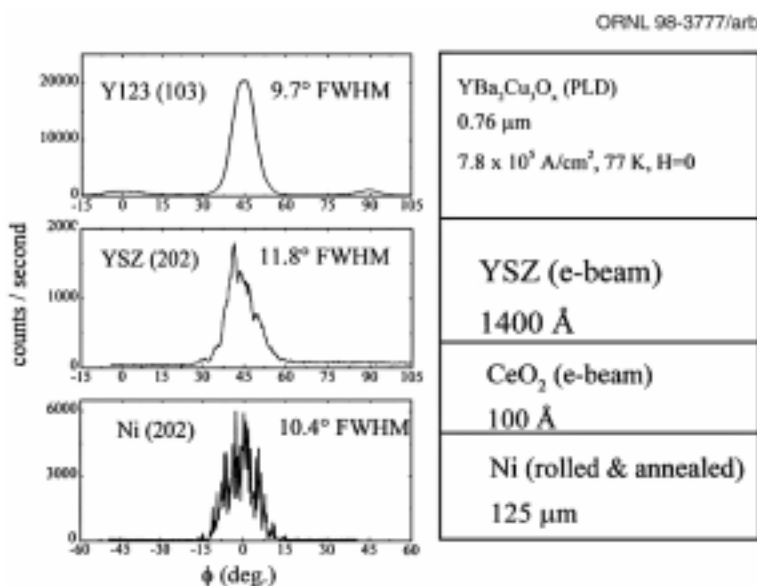
Fig. 1.18. The φ scans for a 0.76-µm-thick YBCO deposited on 1400-Å-thick YSZ-buffered Ni at 780°C.

presence of a good in-plane texture. The films were further characterized by resistivity and transport I_c measurements using a conventional four-probe technique. Values of transport J_c were calculated using a 1-µV/cm criterion. The temperature dependence of both critical currents, I_c and J_c, values for 0.76-µm-thick YBCO films are shown in Fig. 1.19. A maximum J_c of 7.8×10^5 A/cm^2 was obtained at 77 K and zero field. At 75 K, a J_c of about 1×10^6 A/cm^2 was obtained. These results show that high J_c YBCO films can be grown on 1500-Å-thick buffer layers.

ORNL 98-3987/arb

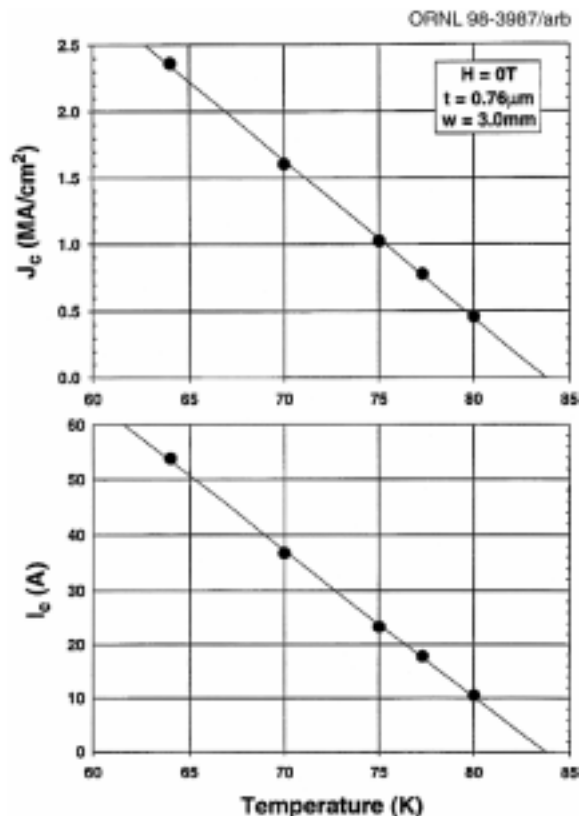**Fig. 1.19. The temperature dependence of both I_c and J_c values for a 0.76-µm-thick YBCO film.**

DEVELOPMENT OF HIGH-J_C HTS COATINGS BY PRECURSOR-DEPOSIT APPROACHES

Background

A technically and economically viable coated-conductor technology will require the development of techniques to rapidly coat biaxially textured, buffered metal tapes with thick, high-J_c HTS deposits. While work is in progress to develop YBCO coatings by the highly scalable solution techniques, to date high-J_c deposits on metal tapes have been achieved only by vapor deposition methods, such as PLD and metallo-organic chemical vapor deposition (MOCVD). The present work focuses on issues related to the scale up of coatings by a new approach to vapor-deposited coated conductors that combines some attractive features of both vapor and bulk coating techniques.

The production of vapor-deposited HTS films may be regarded as occurring by two general approaches: in situ or ex situ processing. In the in situ approach, the deposition conditions are controlled in such a way that a completely formed, biaxially aligned HTS coating is grown during the deposition. In the ex situ approach, an amorphous or micro-crystalline precursor film is deposited, containing all or some of the components of the final HTS compound, in much the same way as the solution approaches. This precursor deposit should be chemically and structurally robust because formation of the HTS compound may be conducted ex situ in a (batch) furnace anneal in which the components are reacted, with additional necessary components possibly provided via the vapor phase. For a wire technology, the ex situ approach has several advantages: (1) during deposition of the precursor film, there is no need to maintain the moving tape substrate at high temperature or to provide a source of activated oxygen; (2) in principle, there is no growth-rate limitation to the deposition rate of the precursor film; and (3) the reaction to form the fully HTS

wire might be conducted by large-scale batch annealing, which is not rate-limited by linear processes.

Objectives and Approach

Here we report results of studies to develop methods for the vapor deposition of high-J_c YBCO and Tl1223 coatings using the precursor approach. Compared with Bi-based HTS conductors, both these HTS materials exhibit superior flux pinning properties in the presence of magnetic fields at liquid nitrogen temperatures (64–77K) and would open new applications for HTS coated conductors at these high temperatures. In these initial studies, we have focused on the compatible growth of high-J_c films on single crystal substrates that comprise the upper layers of the present RABiTS™ architecture and on a demonstration that such films can be grown to the thicknesses needed for a conductor technology.

The work on YBCO films was conducted as part of a CRADA partnership with the 3M Company, Southwire Company, and LANL and exploits the deposition of Y-BaF_2-Cu precursor films by e-beam co-evaporation, a deposition technology that is already used extensively for product fabrication by 3M. The project draws on expertise developed during several years of base program research at ORNL, where parameters were developed for the production of high-quality thin films, primarily on single crystal $SrTiO_3$ and $KTaO_3$ substrates. In this technique, the precursor films are chemically and mechanically stable and can be readily stored for extensive periods until the ex situ reaction anneal, conducted at 740–780°C in an $O_2/H_2O/N_2$ gas mixture at low oxygen partial pressure. The principal objective of this task was to extend the technique to thick coatings that retain full epitaxy and c-perpendicular alignment. A related specific objective was to understand the processes underlying the formation of these thick films and to begin to optimize the process for use with RABiTS™.

The research on Tl1223 films involved a collaboration with researchers at the State University of New York (SUNY) at Buffalo, who had previously developed ex situ processing techniques to produce high-J_c epitaxial films of $Tl_{0.78}Bi_{0.22}Sr_{0.6}Ba_{0.4}Ca_2Cu_3O_{9-\delta}$ (TlBi1223) on substrates of single crystal $LaAlO_3$. In this case, the Tl-free precursor films are deposited by PLD, and the reaction anneal occurs in a two-zone furnace in the presence of flowing O_2 and Tl_2O vapor. The principal objective was to find parameters appropriate to produce ~1-µm-thick, high-J_c films on single crystal YSZ, the same oxide that comprises the upper buffer layer of the RABiTS™ architecture. Initial results of deposition on RABiTS™ were also evaluated.

Results

Thickness Dependence of J_c for Ex Situ YBCO Films

In these controlled studies, precursor films of various thicknesses were deposited by e-beam co-evaporation of Y, BaF_2, and Cu onto single crystal $SrTiO_3$ substrates in order to find processing parameters suitable to produce thick, c-perpendicular-oriented epitaxial films and to document the systematic dependence of J_c on thickness. Despite numerous claims in the early literature that the c-perpendicular orientation is unstable for growth to thicknesses greater than a few thousand angstroms, we were able to synthesize fully epitaxial films exceeding 1 µm in thickness. This success depends strongly on the groundwork of earlier research where the importance of low oxygen pressure during the reaction process was identified. In the present work, typical processing conditions are $p(O_2) \approx 200$ mtorr, $p(H_2O) \approx 20$ torr, at a reaction temperature of 780°C for a duration of about 1 h. Results for J_c as a function of thicknesses to ~1.3 µm, in the liquid nitrogen temperature range, are shown in Fig. 1.20, both at self field and for a 1-Tesla field applied parallel to the c-axis. The curve in Fig. 1.20 represents the J_c

ORNL 98-3931/arb
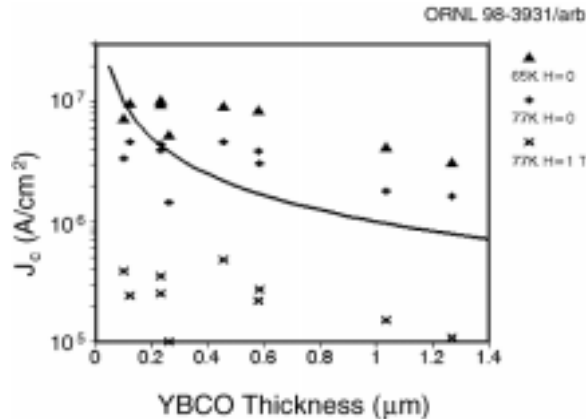
Fig. 1.20. The J_c at liquid nitrogen temperatures as a function of film thickness for epitaxial YBCO on SrTiO$_3$, processed by the ex situ technique described. Results are shown at zero applied field and for 1-Tesla fields applied parallel to the *c* axis.

levels required to achieve the proposed operations criterion for a tape conductor with a sheet current of K_c>10 A/mm-width. Whereas the present data may indicate some degradation of J_c with thickness, low-field values remain well above the K_c criterion. Because structural studies (XRD and ion beam RBS) indicate good crystalline order, work in progress will determine if the fall off is related to a paucity of flux pinning defects as the films become more bulk-like with thickness. Additional important issues are the effects of practical substrate (buffer layer) materials on the compatibility with the ex situ processing requirements; development of ex situ YBCO films on CeO$_2$ and YSZ buffer layers is under way, for ultimate compatibility with the full RABiTS™ tapes.

### *Development of Epitaxial TlBi1223 Films on YSZ Surfaces*

Previously, the reaction post-anneals to form high-J_c epitaxial films of TlBi1223 on single crystal LaAlO$_3$ were conducted either in air or oxygen at temperatures near 860°C. These processing conditions may be incompatible with the reactive base-metal substrates of RABiTS™. Moreover, no previous knowledge base had

existed for the epitaxial growth of TlBi1223 on YSZ, which is a present upper-surface buffer layer of RABiTS™. In this work we were able to successfully synthesize fully epitaxial films at greatly reduced oxygen pressure and temperature. The present films, 0.7 µm thick, are processed in proximity to unreacted TlBi1223 pellets and in-flowing argon and Tl$_2$O vapor at 780°C for 40 min. The processing temperature and ambient conditions are comparable with those of the ex situ YBCO synthesis and those of in situ depositions that have shown compatibility with RABiTS™. The films contain a small amount of epitaxial TlBi1212 second phase, as determined by XRD, but otherwise are well ordered, with both in-plane and out-of-plane alignments of less than 1.5° FWHM.

Transport measurements show a zero-resistance transition temperature of about 108 K. In Figs. 1.21 and 1.22, results of transport J_c are given, showing the temperature dependence in self-field and the field-dependent J_c at 77 K and 64 K (just above the triple point temperature of liquid nitrogen), respectively. In zero applied field, the J_c value at 77 K is about 1.1 MA/cm^2 and is nearly 2 MA/cm^2 at 64 K. Comparison with a high-J_c YBCO film illustrates an attribute of TlBi1223—the expanded high-temperature operation range, evidenced by a J_c of 10^5 A/cm^2 near 100 K,

ORNL 98-3932/arb
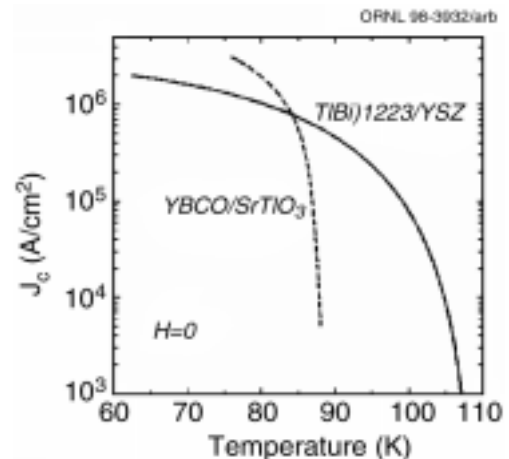
**Fig. 1.21. The J_c measured in self-field.** The dashed line is data for a high-J_c YBCO film on SrTiO$_3$.
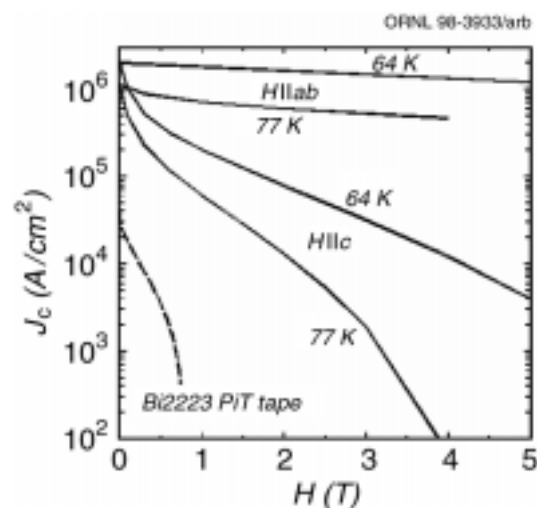
Fig. 1.22. The magnetic field dependence of J_c, for field orientations both parallel ($H\|ab$) and perpendicular ($H\|c$) to the film plane, for the two temperatures 64 K and 77 K spanning the useful LN$_2$ range. For comparison, data for commercial Bi2223 powder-in-tube tapes are included.

where YBCO is no longer superconducting. The field-dependent measurements clearly illustrate the advantages of TlBi1223 films over present state-of-the-art Bi2223 tapes. Of course, the important outstanding issue is the extension of these results to RABiTS™. Results of such an
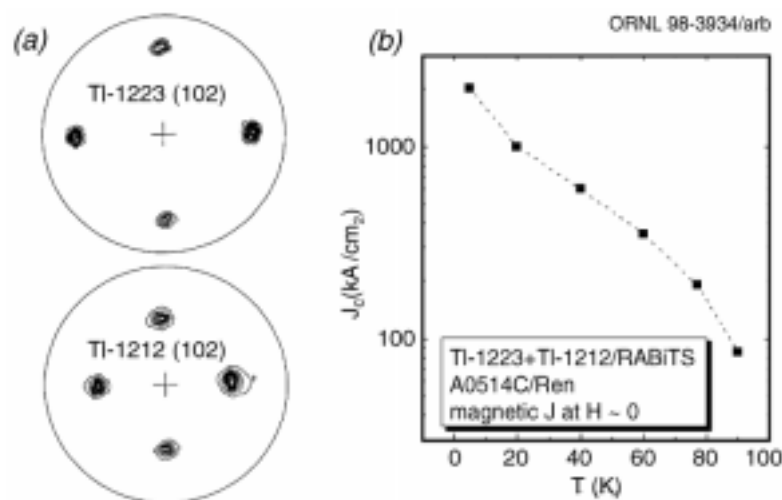
initial attempt are shown in Fig. 1.23, where techniques similar to the above were employed to deposit the films on a RABiTS™ of architecture YSZ/CeO$_2$/Ni. The X-ray (102) pole figures of Fig. 1.22 show that the sample is mixed phase, with nearly equal distribution of epitaxial TlBi1212 and TlBi1223. Results of the low-field $J_c(T)$ for this small sample were deduced from magnetic hysteresis measurements and yield a low-field (trapped flux) value $J_c(77\ \text{K}) \approx 200$ kA/cm^2 at 77 K. This first result offers encouragement for further development of TlBi1223 coatings on RABiTS™. Work is also under way to refine the processing parameters for 1223 on CeO$_2$ buffers, which also can be used as the RABiTS™ upper surface.

Summary and Conclusions

Vapor deposition techniques (e-beam co-evaporation and PLD) have been used to deposit precursor films of YBCO and Tl1223, respectively. In both cases, the films are converted to the superconducting phase by an ex situ furnace post-annealing process. Investigations of the YBCO films deposited on single crystal substrates have shown that epitaxy, c-perpendicular alignment, and good superconducting transport properties can be achieved to thicknesses greater than 1 µm. For the TlBi1223 material, high-J_c films on YSZ surfaces have been developed through modification of the ex situ processing to lower the reaction temperature from ~860 to ~760°C and to greatly reduce the oxygen partial pressure. An initial attempt to employ this approach to deposition of TlBi1223 on a RABiTS™ gave encouraging results. These results help demonstrate feasibility of the ex situ approach and provide further motivation for its development as the HTS layer in a coated-conductor technology.

Fig. 1.23. (*a*) The XRD (102) pole figure of a Tl film on RABiTS™, showing the epitaxial co-existence of 1223 and 1212 phases. (*b*) The J_c in low field determined from magnetization hysteresis.

FIRST DEMONSTRATION OF A LONG LENGTH RABiTS™

Scale-up experiments under way at ORNL are designed in part to provide longer lengths of RABiTS™ for YBCO deposition at ORNL, LANL, and Midwest Superconductivity, Inc. Recently, over 30-cm-long CeO_2-buffered, textured-Ni substrates were fabricated for the first time using a rotating cylinder in an e-beam evaporator. Also, we fabricated a RABiTS™ over 6-cm long with a layer sequence of YSZ (1000 Å)/CeO_2 (400 Å)/Ni (125 μm) in a static mode in the e-beam system. Detailed XRD analysis on this long substrate showed that the FWHM values for the top YSZ layers were 9–10° [in-plane epitaxy; (202) φ scan] and 6–7° [out-of-plane epitaxy; (002) ω scan]. Attempts are being made to grow YBCO on these substrates.

In an attempt to scale up our RABiTS™ process, we proceeded in two ways. The first approach is the simple mounting of long textured Ni on a heating stage in a static mode in the e-beam system. The second approach is to wind textured Ni on a rotating cylinder that can be mounted inside the e-beam system. By using the first approach, we fabricated a RABiTS™ over 6-cm long with a layer sequence of YSZ (1000 Å)/CeO_2 (400 Å)/Ni (125 μm) using our e-beam evaporator. Detailed X-ray analyses were made on three different spots. The results indicated that the top YSZ layer had FWHM values of 9–10° [in-plane epitaxy; (202) φ scan] and 6–7° [out-of-plane epitaxy; (002) ω scan]. The film appeared to be golden yellow in color. We also fabricated a rotating copper cylinder with a heating assembly that can be mounted in

the e-beam system. The cylinder is convenient for winding 1.8 m of 1.0-cm-wide Ni tapes, can be rotated from 0 to 360° at ~8 rpm, and can be heated up to 800°C. Using this rotating cylinder, we have recently demonstrated that over 30-cm-long CeO_2-buffered Ni substrates can be made (see Fig. 1.24). The thickness of the CeO_2 layer was 1000 Å. The film appeared to be blue in color and the thickness appeared to be uniform throughout the sample. Attempts will be made to grow YBCO on these long substrates.

OXFORD CRADA: Bi-2212 CONDUCTOR DEVELOPMENT

Conductor Insulation Materials

Dip-coated Bi-2212/Ag conductors are being developed for high-field insert coil applications. Producing the coils by winding followed by subsequent reaction has the advantage of avoiding cracking degradations that occur when prefired conductors are wound into coils. The difficulties with the wind-and-react process involve removing the organic dip-coating compounds and reactions between the liquid phase formed during partial melting and the oxide electrical insulation. Both Al_2O_3 and ZrO_2 react rapidly with the liquid formed when Bi-2212 melts, and the reaction products degrade conductor performance and reduce electrical insulation.

Compatibility tests have shown that $CaZrO_3$, $SrZrO_3$, and $BaZrO_3$ do not react with the Bi-2212 liquids, and a preliminary evaluation indicates that they may be useful for wind-and-react coils. Coils insulated with low density

ORNL 98-3988/arb

Fig. 1.24. First demonstration of an ~30-cm-long CeO_2-buffered Ni substrate using a rotating cylinder in the e-beam evaporator. Ni substrate = 5 mil; CeO_2 thickness = 1,000 Å.

$CaZrO_3$ powder were compared with Al_2O_3 paper-insulated coils. Measurements showed the $CaZrO_3$ coils had approximately two times higher resistances between conductor turns. Higher density zirconate coils are now being investigated.

Removal of CO_2 from Silver-Clad BSCCO Conductors

This study was initiated to experimentally determine if it is possible to remove CO_2 gas from inside Ag-clad BSCCO conductors. Carbonate ions can be accommodated in the BSCCO lattices and the partial melting process step can result in CO_2 evolution and conductor bubbling. These defects have been observed at carbon levels as low as 600 ppm. The difficulties have been discussed in detail by Hellstrom and Zhang.[1]

Moisture and excess oxygen can also cause bubble formation, but these species can be removed by vacuum drying and oxygen diffusion through the Ag clad. Evolution of CO_2 is a more intractable problem because it is mostly retained in the BSCCO lattice until partial melting occurs. Clearly, thorough decarburization of the starting BSCCO powder is the best solution to the problem, but attempts to accomplish this have not always met with success. Another possibility is to develop a heat treatment cycle that would allow the CO_2 to permeate through the Ag sheath at temperatures just below the partial melting regime. Theoretical considerations indicated that carbon removal by high temperature diffusion was highly unlikely, but the problem is so serious that an experimental test was performed.

The experiments involved heating sealed Ag capsules and controls in flowing He and ambient air at temperatures between 800 and 900°C. The capsules were filled with dried $CaCO_3$ and $SrCO_3$ and sealed off by e-beam welding. Thermodynamic calculations[2] indicate that at 900°C, the CO_2 pressures over $CaCO_3$ and $SrCO_3$ are 1.04 and 0.053 atm. Compounds and test temperatures were matched to avoid

positive internal pressures. The wall thickness of the Ag capsules was 1 mm and the carbonates comprised 7–8% of the mass. All of the Ag components were vacuum annealed for 4 h at 500°C before the capsules were filled and sealed. The balance sensitivity (10 µg) equals about 4 ppm of the carbonate mass.

The He data are shown in Fig. 1.25 and the air data are shown in Fig. 1.26. On these plots, negative values indicate that the capsules lost more weight than the controls. The step change in the 850°C air data was caused by the capsule sticking to an alumina boat. Processes that might produce a weight change include oxygen pickup, sublimation of Ag, and CO_2 loss. Results in air and He are similar, indicating that oxygen pickup was not a problem. This also shows that the external oxygen pressure has little effect. Sublimation was significant and maximum weight losses at 900°C were 600–650 ppm. If CO_2 losses were significant, the capsules would be expected to lose weight more rapidly than the controls, the effect would become stronger at high temperatures, and the differences in capsule and control weights would increase with time. The data show none of these trends, and the maximum weight difference observed corresponds to only about 0.15% of the available CO_2.

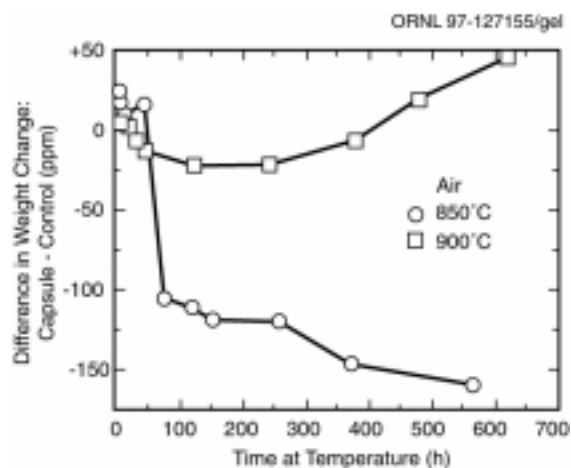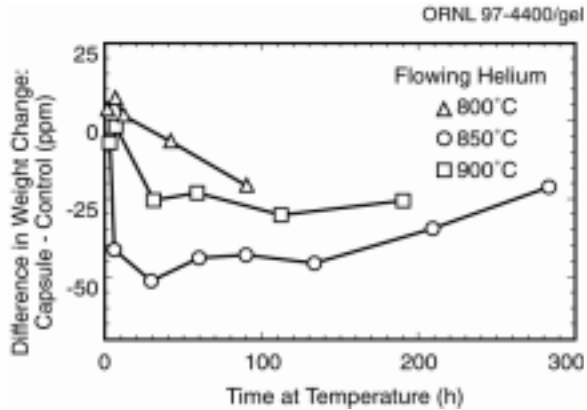A negative cannot be proved; but our data show that, for conditions near those encountered

Fig. 1.25. Differential weight loss for Ag encapsulated carbonates in flowing He.

Fig. 1.26. Differential weight loss for Ag encapsulated carbonates in air.

in conductor processing, CO_2 cannot be removed by diffusion through the cladding. This is consistent with observations that (1) CO_2 does not react with Ag[3] and (2) the maximum solubility of carbon in liquid silver is only 22 ppm.[4]

References

1. E. E. Hellstrom and W. Zhang, *Supercond. Sci. Technol.* **8,** 317 (1995).

2. O. Kubaschewski and C. B. Alcock, pp. 274, 275, 312 in *Metallurgical Thermochemistry*, 5th ed., Pergamon Press, New York, 1979.

3. E. Fromm and E. Gebhardt, p. 678 in *Gase und Kohlenstoff in Metallen*, Springer-Verlag, Berlin, 1976.

4. M. Hansen and K. Anderko, p. 11 in *Constitution of Binary Alloys*, McGraw-Hill, New York, 1958.

GROWTH OF TlBa$_2$Ca$_2$Cu$_3$O$_{9-y}$ SUPERCONDUCTING FILMS ON HIGH-STRENGTH SUBSTRATES USING A SPRAY PYROLYSIS TECHNIQUE

In continuation of our effort to grow TlBa$_2$Ca$_2$Cu$_3$O$_{9-y}$ (Tl-1223) films on metallic substrates using a two-step process, we initiated our work on high-strength oxidation resistant substrates. We have recently developed a technique for bonding Ag to a suitable metal alloy. The typical deposited conductor geometry is shown in Fig. 1.27. The main purpose was to reduce the amount of Ag needed and also to increase the mechanical strength of the substrate. The high-strength substrate also has a smaller thermal expansion mismatch with Tl-1223 as compared with that of Ag and Tl-1223 films. It is also nonmagnetic and has a mechanical strength that is ten times that of pure Ag. The approximate thickness of the high-strength substrate varied from 5 to 10 mil. The typical size of the substrates was 5-mm wide and 1-in. long, and the texture of the substrates was random.
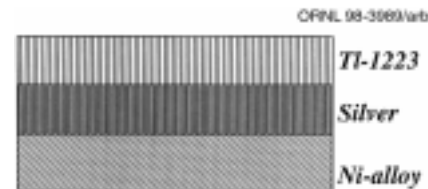
Fig. 1.27. The deposited conductor geometry of high-strength substrates.

Initially, thallium-free precursor films with the composition Ba$_2$Ca$_2$Cu$_3$Ag$_{0.37}$O$_7$ were deposited on the high-strength substrate. The precursor films obtained were smooth and continuous. Thallination was carried out using a standard two-zone thallination furnace with a source temperature of 730°C and a sample temperature of 860°C for 30 min in flowing oxygen. The resulting TlBa$_2$Ca$_2$Cu$_3$O$_{9-y}$ films were black. The film thickness was approximately 3 μm. X-ray powder diffraction studies showed that the films were highly *c*-axis oriented. Values of transport J_c were calculated

using a 1 µV/cm criterion. The magnetic field dependence of the J_c for 3-µm-thick $TlBa_2Ca_2Cu_3O_{9-y}$ films on high-strength substrates is shown in Fig. 1.28. The J_c values were ~52,000 A/cm^2 at 77 K and zero field. At 0.5 T and 77 K, the respective J_c values were 9,800 A/cm^2 and 4,400 A/cm^2 for magnetic field applied parallel and perpendicular to the substrate.
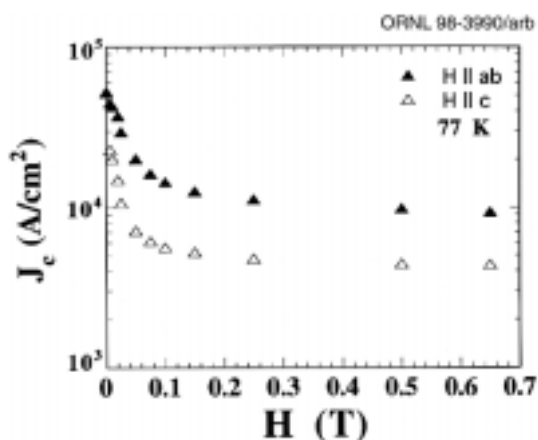

Fig. 1.28. The in-field dependence of J_c for $H\|ab$ and $H\|c$ orientation of 3-µm-thick $TlBa_2Ca_2Cu_3O_{9-y}$ films grown on high-strength substrates at 77 K.

EPITAXIAL GROWTH OF BaZrO$_3$ ON SINGLE CRYSTAL OXIDE SUBSTRATES USING SOL-GEL ALKOXIDE PRECURSORS

In continuation of our effort to develop a nonvacuum process to produce coated conductors, we used the sol-gel alkoxide precursor route in the present study. Also, this report is mainly focused on the development of sol-gel chemistry for BaZrO$_3$ precursors and the feasibility of growing epitaxial thin films on single crystal oxide substrates. BaZrO$_3$ has been considered as a potential buffer layer on textured-Ni substrates to grow YBCO coated conductors. BaZrO$_3$ has been known to form as an intermediate layer while growing YBCO directly on YSZ layers. Also, BaZrO$_3$ is a simple cubic perovskite with a lattice parameter of

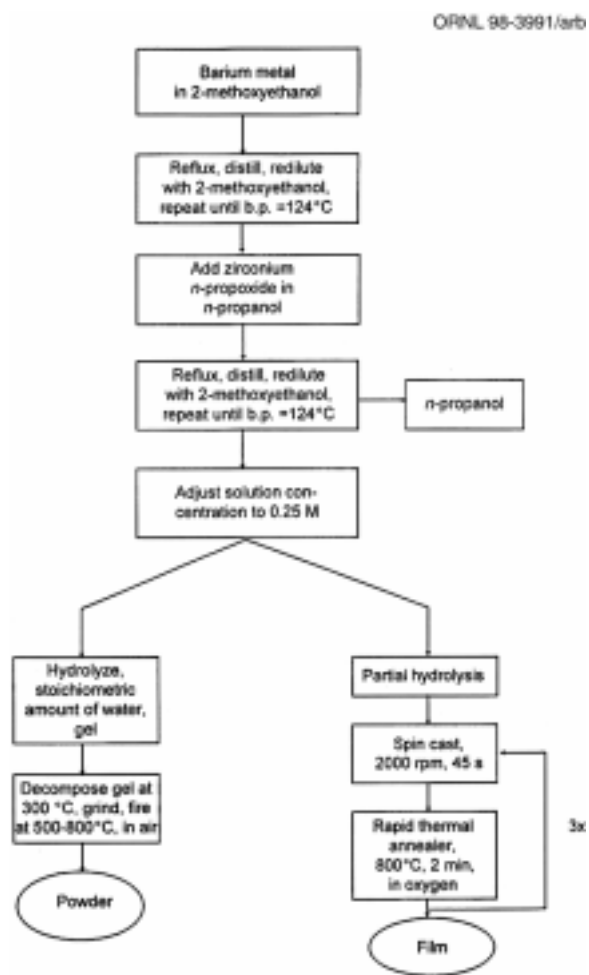4.193 Å. We developed the sol-gel chemistry for BaZrO$_3$ precursors and also demonstrated that the BaZrO$_3$ films can be grown epitaxially on SrTiO$_3$ (100) and LaAlO$_3$ (100) substrates.

The starting reagents were weighed in an argon-filled, inert-atmosphere glove box, and the solution preparation was carried out under argon using standard Schlenk-type apparatus. Barium metal (Alfa, 99.99%), zirconium n-propoxide in n-propanol (Alfa, 70%), and 2-methoxyethanol (Alfa, spectrophotometric grade) were used without further purification. The flowchart for the preparation of BaZrO$_3$ precursors is given in Fig. 1.29.

Barium metal (0.858 g, 6.25 mmol) was allowed to react with 50 mL of 2-methoxyethanol. The barium metal dissolved completely within a few minutes of reflux by evolving hydrogen, and a clear-white barium methoxyethoxide solution was obtained. A stoichiometric amount of zirconium n-propoxide (2.935 g, 8.96 mmol) was then added to the barium solution. Approximately 25 mL of n-propanol/2-methoxyethanol were distilled off, and the solution was repeatedly rediluted with 25–30 mL of fresh 2-methoxyethanol and further distilled for approximately 2 h to again ensure complete exchange of propoxide by the methoxyethoxide ligand. The final volume of the yellow-colored solution was adjusted with 2-methoxyethanol to 50 mL to make a 0.25 M BaZrO$_3$ precursor solution. A partially hydrolyzed solution suitable for spin-coating was prepared by adding approximately 1 equivalent of water (1M H$_2$O in 2-methoxyethanol) per cation equivalent. The solution was allowed to age overnight at room temperature prior to the coating process. Part of the starting precursor solutions were fully hydrolyzed, and the resulting gels were dried on a hot plate. The powders thus obtained were used for the differential thermal analysis (DTA) and thermogravimetric analysis (TGA).

The substrates used for coating in this study were SrTiO$_3$ (100), LaAlO$_3$ (100), and sapphire (polycrystalline) (Commercial Crystal

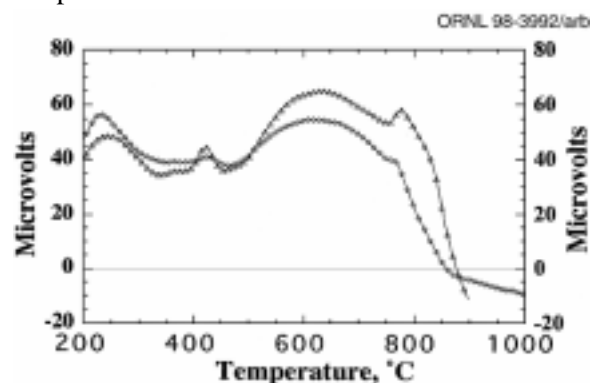The films were analyzed by detailed XRD studies. A Philips Model XRG3100 diffractometer with Cu K_α radiation was used to record the powder diffraction pattern. A Rigaku rotating anode X-ray generator was used, with a graphite monochromator selecting Cu K_α radiation and slits defining a 2×2 mm incident beam. A four-circle diffractometer was used to collect pole figures to measure rocking curves (ω scan) of (002) planes of the (001) textured film, which measure the out-of-plane alignment. The diffractometer was also used to measure ϕ scans of the (101) planes. These scans indicate the in-plane alignment of the film. SEM micrographs were taken using a Hitachi S-4100 field emission SEM. The beam voltage used was 15 kV. The DTA and TGA data were obtained on $BaZrO_3$ powders in both air and oxygen atmospheres in a Sinku-Riko TFD7000 RH instrument. The DTA scan for the same is shown in Fig. 1.30. The main exothermic event took place between 750 and 800 °C in both air and oxygen atmospheres. Hence, the $BaZrO_3$ films were post-annealed around these temperatures.

ORNL 98-3991/arb

Fig 1.29. Flowchart for the preparation of $BaZrO_3$ precursors.

ORNL 98-3992/arb

Fig. 1.30. DTA analysis of the pyrolyzed $BaZrO_3$ gel in air ($\triangle$) and in oxygen ($\Diamond$). The scan rate used was 10 °C/min.

Laboratories, Inc., 1 cm $\times$ 1 cm size, ~0.5-cm thick, one side epi-polished). After the substrates were cleaned ultrasonically in ethanol for a few minutes, three coatings of the partially hydrolyzed precursor solution were made using a spin-coater operated at 2000 rpm for 45 s. Between each coating, the substrate was pyrolyzed in oxygen in a rapid thermal annealer (RTA, AG Associates Model 610) at 800 °C for 2 min. The total thickness of the resulting film was approximately 300 nm.

The room temperature powder XRD pattern for 300-nm-thick $BaZrO_3$ films grown on both sapphire and $LaAlO_3$ substrates are reported in Figs. 1.31 and 1.32. Figure 1.31 shows the presence of a polycrystalline $BaZrO_3$ film
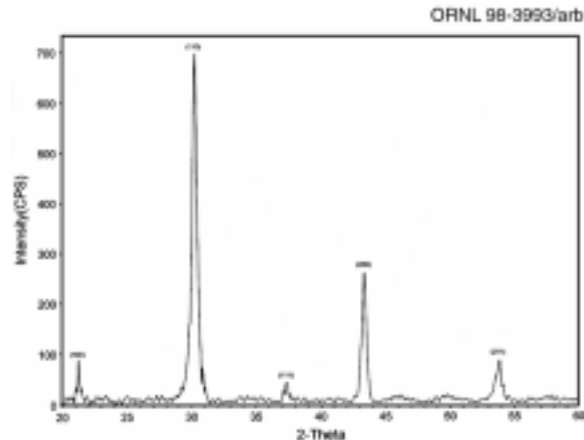
Fig. 1.31. The room-temperature powder XRD for 300-nm-thick BaZrO$_3$ films grown on sapphire substrates.
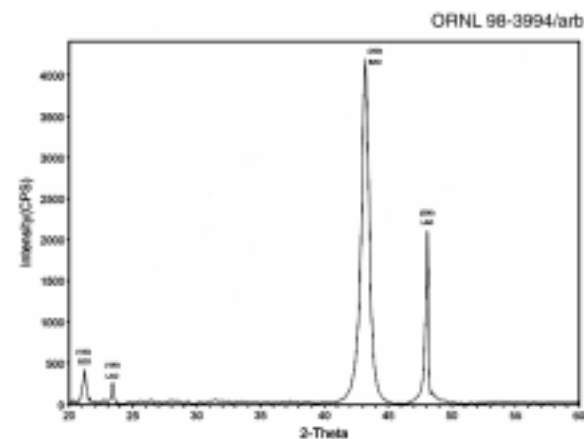

Fig. 1.32. The room-temperature powder XRD for 300-nm-thick BaZrO$_3$ films grown on LaAlO$_3$ (100) substrates. The film shows the *c*-axis alignment.

whereas Fig. 1.32 indicated the presence of a c-axis texture on LaAlO$_3$ substrates. Similar *c*-axis texture was also obtained on SrTiO$_3$ substrates. XRD results from the ω and φ scans for films grown on both SrTiO$_3$ and LaAlO$_3$ substrates revealed (100) cube texture. The FWHM values for BaZrO$_3$ films on SrTiO$_3$ substrates were 1.8° (out-of-plane epitaxy) and 2.6° (in-plane epitaxy). Similarly, the FWHM values for films grown on LaAlO$_3$ substrates were 3.1° (out-of-plane) and 5.0° (in-plane). The sharp texture on SrTiO$_3$ substrates can be

explained in terms of a reduced lattice mismatch. The SrTiO$_3$ has a lattice mismatch of 6.9% with BaZrO$_3$ whereas the LaAlO$_3$ has a mismatch of 9.5% with BaZrO$_3$. A typical φ scan for a 300-nm-thick BaZrO$_3$ film grown on a SrTiO$_3$ substrate is shown in Fig. 1.33. A typical (220) pole figure for a 300-nm-thick BaZrO$_3$ film grown on a SrTiO$_3$ substrate is shown in Fig. 1.34. Figures 1.33 and 1.34 indicate the presence of a single cube-on-cube texture. The BaZrO$_3$ films grown on these substrates were smooth, crack-free, and continuous.
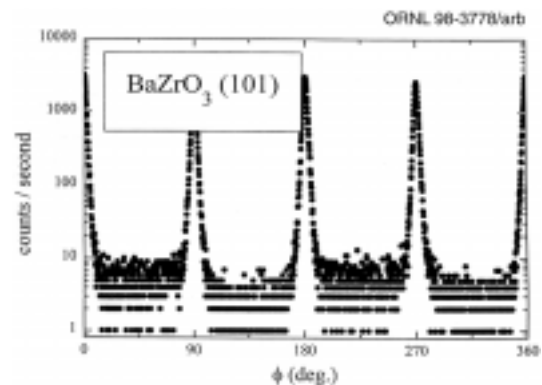

Fig. 1.33. A typical φ scan featuring the epitaxial nature of BaZrO$_3$ films on SrTiO$_3$ (100) substrates.
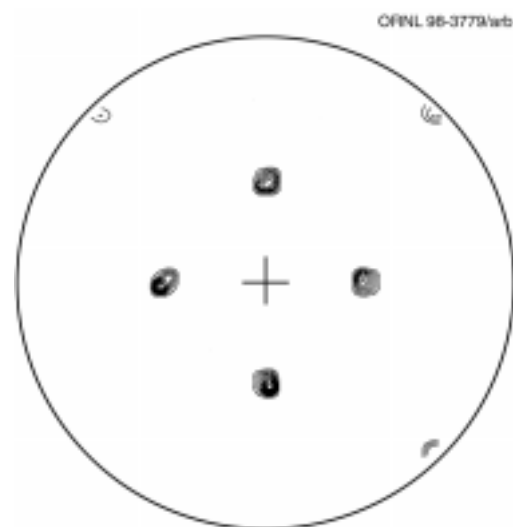

Fig. 1.34. A typical BaZrO$_3$ (220) pole figure for a 300-nm-thick BaZrO$_3$ film on SrTiO$_3$ (100) substrates.

In summary, we developed the sol-gel chemistry for BaZrO$_3$ precursors. The precursor solutions were partially hydrolyzed and spin-coated on several substrates. The films were post-annealed in oxygen at 800°C for a total of 6 min in a rapid thermal annealer. The orientation of the BaZrO$_3$ films grown on sapphire substrates were polycrystalline. But the films on SrTiO$_3$ and LaAlO$_3$ substrates had both out-of-plane and in-plane texture. The BaZrO$_3$ films on SrTiO$_3$ substrates had a fairly sharp texture as the result of the presence of a reduced lattice mismatch. Thus we demonstrated the epitaxial growth of BaZrO$_3$ films on single crystal SrTiO$_3$ (100) and LaAlO$_3$ (100) substrates using sol-gel alkoxide precursors. The BaZrO$_3$ precursors developed in the present work may be used for producing epitaxial buffer layers on RABiTS™ for YBCO coated conductors.

GROWTH OF EPITAXIAL LaAlO$_3$ FILMS ON SrTiO$_3$ (100) SUBSTRATES USING A DIP-COATING PROCESS

A dip-coating unit was assembled at ORNL by mounting a translation unit on a support. The dip coater was controlled automatically with a substrate withdrawal velocity of ≤1.0 m/min. The lanthanum aluminum oxide (LaAlO$_3$) sol-gel alkoxide precursor solutions were used to dip-coat strontium titanium oxide (SrTiO$_3$) (100) single crystal substrates. After drying in air, the dip-coated substrates were heat-treated in air at 800°C for 10 min. The film thickness was ~100 nm. The detailed XRD studies indicated the formation of epitaxial LaAlO$_3$ films. The room temperature powder XRD pattern for a 100-nm-thick LaAlO$_3$ film on SrTiO$_3$ (100) substrate showed the presence of a *c*-axis aligned film. XRD results from the ω and φ scans (as shown in Figs. 1.35 and 1.36) revealed a (100) cube texture. The FWHM values were 0.2° (out-of-plane epitaxy) and 0.4° (in-plane epitaxy). The sharp texture indicates the presence of a highly textured LaAlO$_3$ film. A
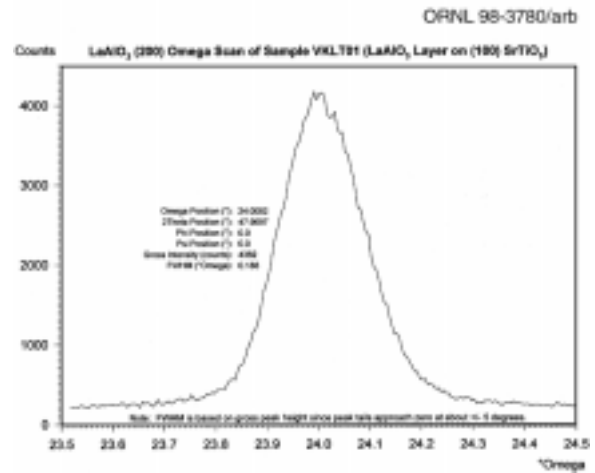

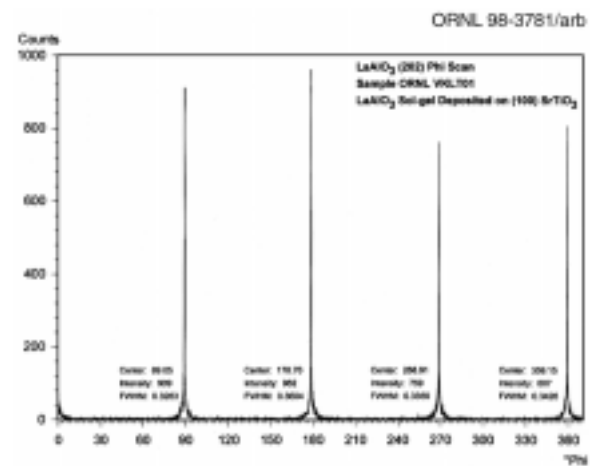**Fig. 1.35. A typical ω scan featuring the epitaxial alignment of LaAlO$_3$ films on SrTiO$_3$ (100) substrates.**

Fig. 1.36. A typical φ scan featuring the epitaxial nature of LaAlO$_3$ films on SrTiO$_3$ (100) substrates.

typical (202) pole figure for a 100-nm-thick LaAlO$_3$ film grown on a SrTiO$_3$ substrate is shown in Fig. 1.37. Figure 1.37 indicates the presence of a single cube-on-cube texture. Thus we reproduced our initial results on spin-coated films with the dip-coated films.

Fresh LaAlO$_3$ precursor solutions were prepared by starting with lanthanum isopropoxide and aluminum sec-butoxide using 2-methoxyethanol as the solvent. The as-prepared solutions were partially hydrolyzed with different degrees of hydrolysis (1:1.0,
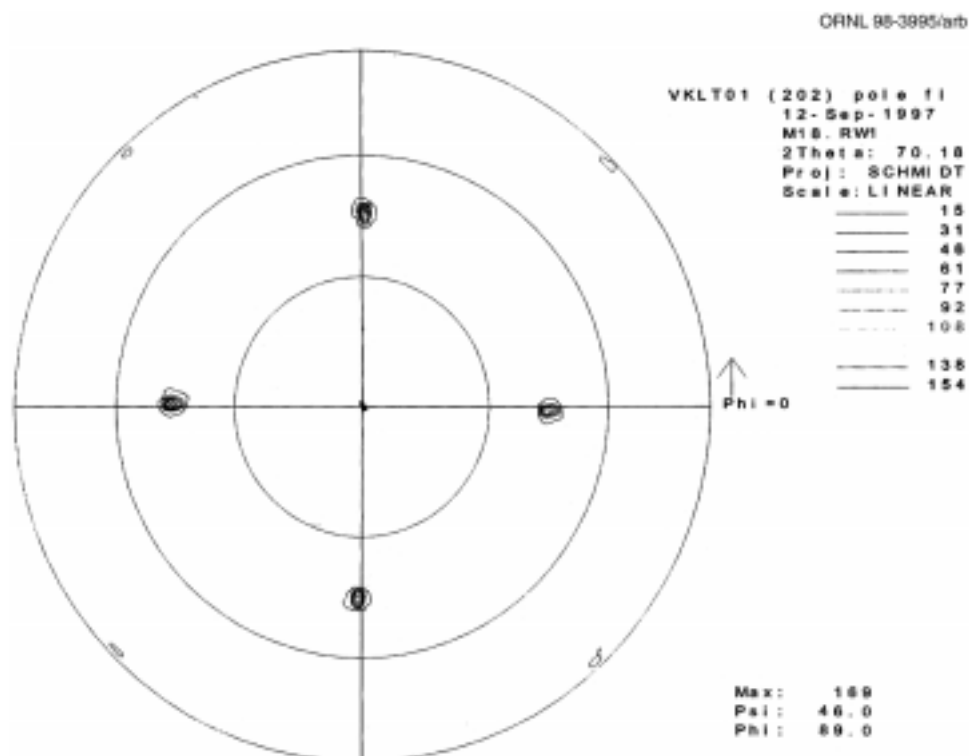
ORNL 98-3995/arb

VKLT01 (202) pole fi
12-Sep-1997
M18. RW1
2Theta: 70.18
Proj: SCHMIDT
Scale: LINEAR

——	15
——	31
——	46
——	61
———	77
———	92
·····	108
——	138
——	154

Phi=0

Max: 169
Psi: 46.0
Phi: 89.0

Fig. 1.37. A typical LaAlO$_3$ (202) pole figure for a 100-nm-thick LaAlO$_3$ film on a SrTiO$_3$ (100) substrate.

1:1.2, and 1:1.4 ratio by volume) using 1M H$_2$O in 2-methoxyethanol. These solutions were dip-coated systematically onto the SrTiO$_3$ (100) single crystal substrates to study the effect of various parameters on the film growth. The parameters varied were substrate withdrawal velocity, degree of hydrolysis, aged solutions, annealing time, atmosphere, and temperature. A set of base conditions was kept constant while one parameter at a time was varied. A complex matrix of 20 different sets of growth conditions was used to grow LaAlO$_3$ films. This study will help us to identify the conditions needed to coat long length substrates. The films were analyzed in detail by XRD. Some of the films were characterized at the University of Tennessee Space Institute X-ray facility. Efforts are now being made to coat LaAlO$_3$ on Ni to see the effect of growth conditions on Ni.

GROWTH OF EPITAXIAL YBa$_2$Cu$_3$O$_{7-x}$ FILMS ON SINGLE CRYSTAL OXIDE SUBSTRATES USING METAL-ORGANIC DECOMPOSITION PRECURSORS
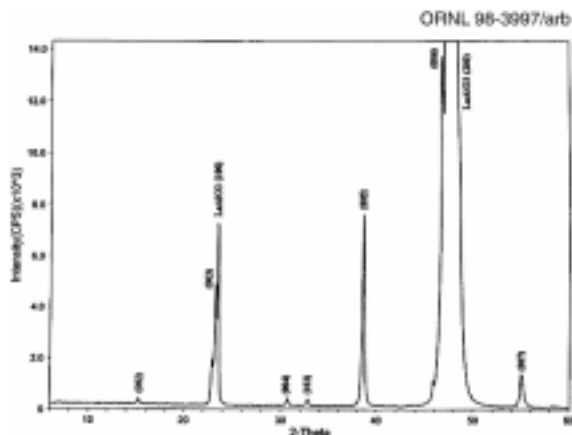
A new metal-organic decomposition (MOD) precursor route for fabricating YBa$_2$Cu$_3$O$_{7-x}$ (YBCO) films was developed in FY 1997. In this process, the starting precursor solution was prepared by dissolving yttrium 2-ethylhexonate, barium neodecaonate, copper 2-ethylhexonate in toluene. The total cation concentration was ~0.14 M. The precursor solution was very viscous. The SrTiO$_3$ (100) and LaAlO$_3$ (100) single crystals were used as the substrates. The flowchart for the preparation of YBCO film is shown in Fig. 1.38.

The YBCO precursor solutions were spin-coated on LaAlO$_3$ substrates at a speed of 2000 rpm for 40 s. A total of five coatings were performed to achieve a thickness of approximately 400 nm. Between each coat, the
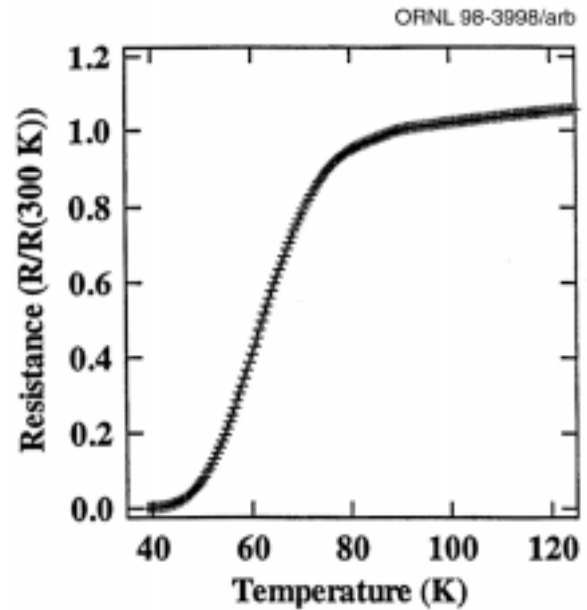
ORNL 98-3996/arb
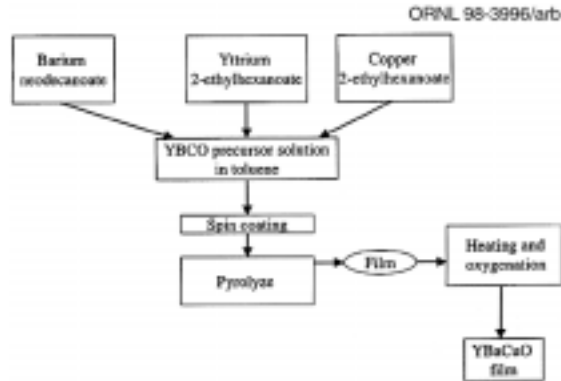
Fig. 1.38. Flowchart for the preparation of YBCO films.

films were pyrolyzed at 400°C for 1 h in air. Slow heating rate (2°/min) was essential to get a continuous film. After five coatings, the film was heated again at 400ºC for 2 h in 1 atm oxygen to remove all the hydrocarbons and then heat treated at 850ºC for 2 h in 2% oxygen. A typical powder XRD pattern for the YBCO film is shown in Fig. 1.39. Figure 1.39 indicates the presence of a c-axis aligned YBCO film on $LaAlO_3$. Similar results were also obtained for films on $SrTiO_3$ substrates. On $SrTiO_3$ substrates, small amounts of a-axis oriented YBCO, CuO, and $BaCuO_2$ impurities were also observed. However, the ϕ scan (102) on the YBCO film on $SrTiO_3$ indicated the presence of a single cube textured film. The resistance vs temperature plot for the YBCO film on a $SrTiO_3$ substrate is shown in Fig. 1.40. The film has a

ORNL 98-3998/arb

Fig. 1.40. The resistivity plot for a 400-nm-thick YBCO film grown on a $SrTiO_3$ (100) substrate.

very broad transition with a zero resistance of 40 K. The SEM image (as shown in Fig. 1.41) reveals the presence of secondary phases along with the YBCO film. This could be one of the reasons for low critical temperatures (T_cs).

ORNL 98-3997/arb

Fig. 1.39. The powder XRD for a 400-nm-thick YBCO grown on a $LaAlO_3$ (100) substrate. The film shows the c-axis alignment.

ORNL 98-3999/arb

Magnification 2.5kX)
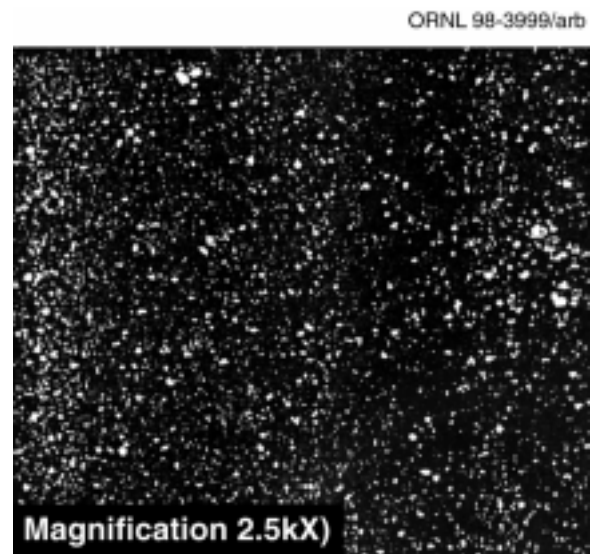
Fig. 1.41. The SEM micrograph for a 400-nm-thick YBCO film grown on a $SrTiO_3$ (100) substrate.

THE GROWTH OF EPITAXIAL BUFFER LAYERS ON SINGLE CRYSTAL OXIDE SUBSTRATES USING SOL-GEL ALKOXIDE PRECURSORS

Novel sol-gel precursor solutions of the perovskite-type compounds $NdAlO_3$, $GdAlO_3$, and $YAlO_3$ have been prepared. These compounds are of interest in part because their lattice parameters are smaller than those of the other more traditional buffer layers, such as $LaAlO_3$ and CeO_2, which may make them better candidates for deposition on Ni when using sol-gel techniques. These aluminate layers also do not have the twinning problems associated with $LaAlO_3$. Epitaxial films of these buffer layers have been grown on single crystal $SrTiO_3$ (100) substrates. The solutions were applied to the substrates by spin coating, and then the substrates were pyrolyzed in O_2 at 800°C for 2 min in a rapid thermal processor. The thickness of the films was increased by multiple coatings and pyrolysis treatments. Each coating yielded approximately 500–1000 Å of film.

A precursor solution of $SrTiO_3$ was made from standard sol-gel procedures using strontium metal and a titanium alkoxide. Epitaxial films of $SrTiO_3$ were grown on $LaAlO_3$ (100) single crystals by both pyrolysis in a rapid thermal processor at 600°C in O_2 for 2 min and by slow heating to 650°C, annealing for 1 h in air, and slow cooling. Again thickness was increased either by cycles of coatings and pyrolysis treatments in the rapid thermal processor or by drying each coat in air for 10 min at 300°C before the 650°C anneal.

Approximately 500 Å resulted from each coating.

The films are strongly *c*-axis oriented as indicated by θ-2θ scans, an example of which is seen in Fig. 1.42. The strong *c*-axis orientation was affirmed by the rocking curve results of the individual (002) planes, and φ scans of the (202) planes, and (111) in the case of $YAlO_3$, confirmed the good in-plane texture. The FWHM values measured from these scans of all the buffer layers are as follows:

$NdAlO_3$ on $SrTiO_3$, out-of-plane=1.5°; in-plane=1.4°
$GdAlO_3$ on $SrTiO_3$, out-of-plane=1.6°; in-plane=2.1°
$YAlO_3$ on $SrTiO_3$, out-of-plane=2.8°; in-plane=3.7°
$SrTiO_3$ on $LaAlO_3$, out-of-plane=1.1°; in-plane=1.6

Pole figure analyses revealed that the films exhibit the desired single orientation cube-on-cube epitaxy of $[100](001)_f \| [100](001)_s$. (See Fig. 1.43.)
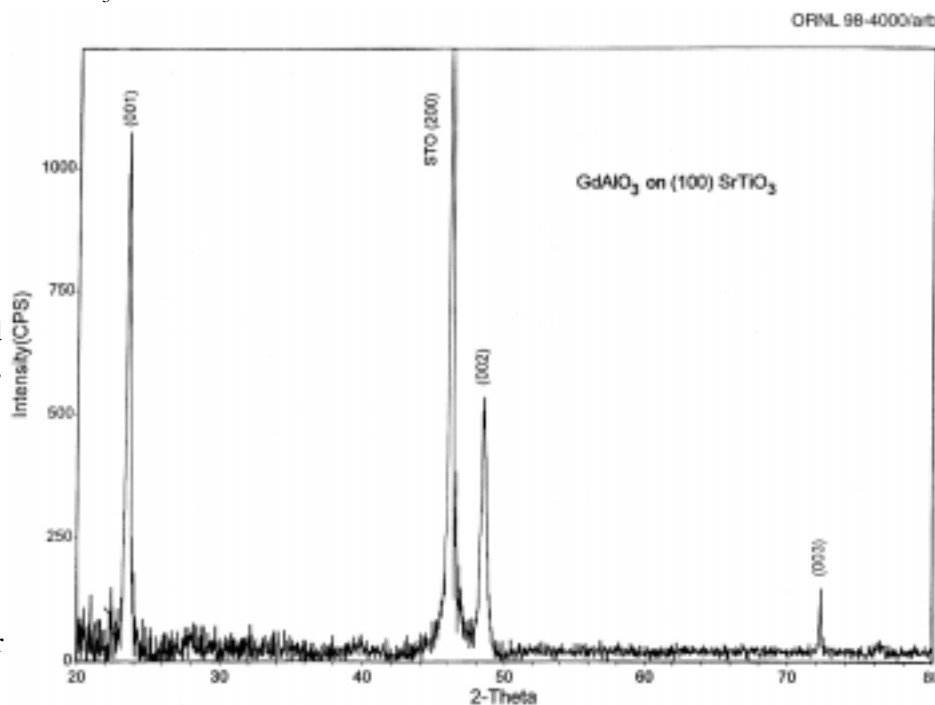

ORNL 98-4000/arb

GdAlO₃ on (100) SrTiO₃

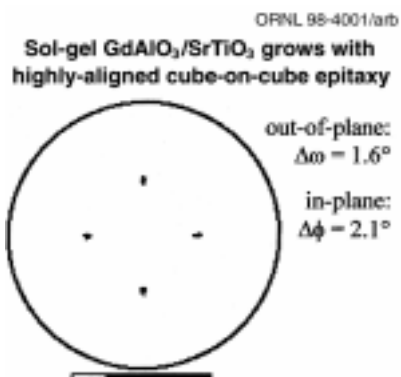**Fig. 1.42.** θ-2θ **scan of GdAlO₃ on a SrTiO₃ (100) single crystal.**

Fig. 1.43. GdAlO$_3$ (220) pole figure.

HIGH-RESOLUTION TEM/AEM CHARACTERIZATION OF EPITAXIAL OXIDE MULTILAYERS FABRICATED BY LASER ABLATION ON BIAXIALLY TEXTURED Ni

The success of RABiTS™ relies on the successful epitaxial deposition of cube-on-cube or rotated cube-on-cube oriented oxide buffer layers on the {100}<100> textured-Ni substrate. This has been accomplished using two methods. First is by epitaxial deposition of an intervening noble metal layer between the oxide and Ni. The second is by epitaxial deposition of the oxide layers directly on Ni under conditions such that formation of NiO is not thermodynamically expected. YBCO films deposited on such substrates have J_cs approaching 3 MA/cm^2 at 0 T and 77 K. We report here the results of a detailed microstructural and compositional examination of oxide buffer layers deposited directly on Ni using laser ablation.

Experimental Procedure

Fabrication of the YBCO Tapes

Biaxially textured Ni substrates were formed by consecutive rolling of a polycrystalline, randomly oriented high purity (99.99%) bar to total deformations greater than 95%, followed by recrystallization. Examination

of (111) and (200) pole figures of an as-rolled Ni tape show localization of intensities along the {112}<111> and the {123}<634> orientations along the β-fiber or the skeleton line, consistent with the formation of a sharp copper-type rolling texture. By controlling the surface condition of the work rolls, it was possible to obtain substrates with surfaces with a rms roughness of ~10 nm. The substrate was then annealed in situ in a laser ablation chamber at 900°C for 2 h in 4% H$_2$ in Ar, resulting in the formation of a sharp {100}<100> cube texture. Typical samples showed X-ray ω- and φ-scans with FWHM of 6° and 7°, respectively. Grain boundary studies of the substrate using electron BKD showed that over 95% of the boundaries had misorientations less than 5°.

Ceramic oxide films were deposited on the biaxially textured Ni substrate using pulsed laser ablation with the substrate held at a constant temperature of 780°C. The multilayer sample studied was of the composition YBCO (1 μm)/YSZ (0.2 mm)/(CeO$_2$) (0.9 μm)/Ni (125 μm). (100) epitaxy of CeO$_2$ was established by performing the initial deposition in 180 mtorr of 4% H$_2$ in Ar to a thickness of ~30 nm. The flow of 4% H$_2$-Ar gas was then stopped resulting in a vacuum of 10^{-5} torr. An additional layer of ~ 50 nm of CeO$_2$ was deposited in this vacuum. Oxygen was then introduced into the chamber and the subsequent deposition of CeO$_2$ was performed in p(O$_2$) ~4 × 10^{-4} torr to a total thickness of 0.9 μm. YSZ was deposited on CeO$_2$ under a p(O$_2$) ~4 × 10^{-4} torr to a thickness of ~0.2 μm. A 1-μm YBCO layer was deposited on the YSZ layer at p(O$_2$) ~180 mtorr. The sample was first cooled to 200°C at 10°C/min and then furnace cooled to room temperature. Grain boundary studies of the substrate using electron BKD showed that most areas had grain boundary misorientations less than 5°.

Electron Microscopy

TEM cross-section samples were prepared by coating the YBCO tape with an ~2-mm-thick copper layer using electrodeposition. The

electrodeposition was performed at room temperature using a diluted sulfuric copper solution (90g $CuSO_4$, 15 mL H_2SO_4, and 475 mL H_2O). Wrapped in a thick layer of copper, the YBCO tape had enough mechanical integrity to be sliced without delamination at the metal–ceramic interface. TEM foils were then prepared by grinding, polishing, dimpling, and ion milling the 3-mm discs cut from the thin slices. A thin carbon coating was applied to the specimen prior to TEM examination to minimize charging. It should be pointed out that the YBCO is not stable in the sulfuric copper solution whereas all the other layers (Ni, CeO_2, and YSZ) are stable. Even though not applicable to samples for characterization of the superconducting materials, this is a simple method to prepare cross-sectional samples for studying the multilayer substrate of the superconductor tape (Ni/CeO_2/YSZ).

Microstructural and microchemical characterizations were performed using both conventional TEM (Philips CM12) and high-resolution analytical electron microscopy (AEM) (Philips CM200). The CM 200 microscope was equipped with a field emission gun (FEG) and an energy dispersive spectrometer (EDS) (Super UTW, Link/Oxford). For high spatial resolution compositional analyses, the microscope was operated in the scanning TEM (STEM) mode with a probe size of 2 nm. Composition profiles across an interface (or a certain region) were collected in the sequential acquisition mode during a single line scan across the interface (or the region) with step sizes of 2–4 nm.

Results and Discussion

General Microstructures

The orientation of the individual layers was determined using selected area diffraction (SAD) patterns, as illustrated by Fig. 1.44. First, the specimen was tilted so that in the region shown in Figure 1.44(*a*), the (100) plane of the Ni substrate, was perpendicular to the electron
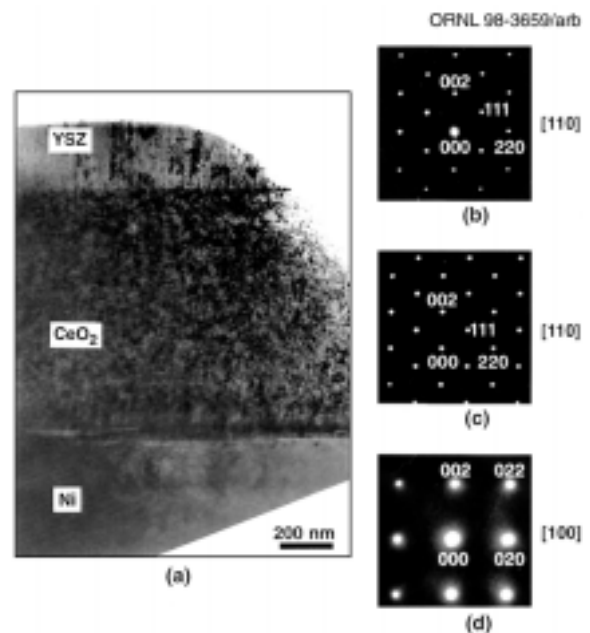
Fig. 1.44. (*a*) General interfacial microstructure of the biaxially textured multilayer substrates and SAD patterns collected from (*b*) the YSZ layer, (*c*) the adjacent CeO_2, and (*d*) the Ni substrate. The low order reflections are indexed, and the upward drawn direction (i.e., the e-beam direction) is indicated beside each diffraction pattern.

beam as indicated by the SAD patterns in Figure 1.44(*d*). SAD patterns of the adjacent CeO_2 and YSZ layer were then recorded under such tilt conditions and are shown in Fig. 1.44(*c*) and (*b*). Indexing the diffraction patterns showed that the lattice planes perpendicular to the incident beam in the CeO_2 and the YSZ layers were the (110) planes. There was a 45° in-plane rotation between the metal substrate and the oxide layers deposited. The SAD patterns also showed that in all the three layers (Ni, CeO_2, and YSZ) the [001] axes were perpendicular to the layered structure, consistent with the biaxial nature of the materials.
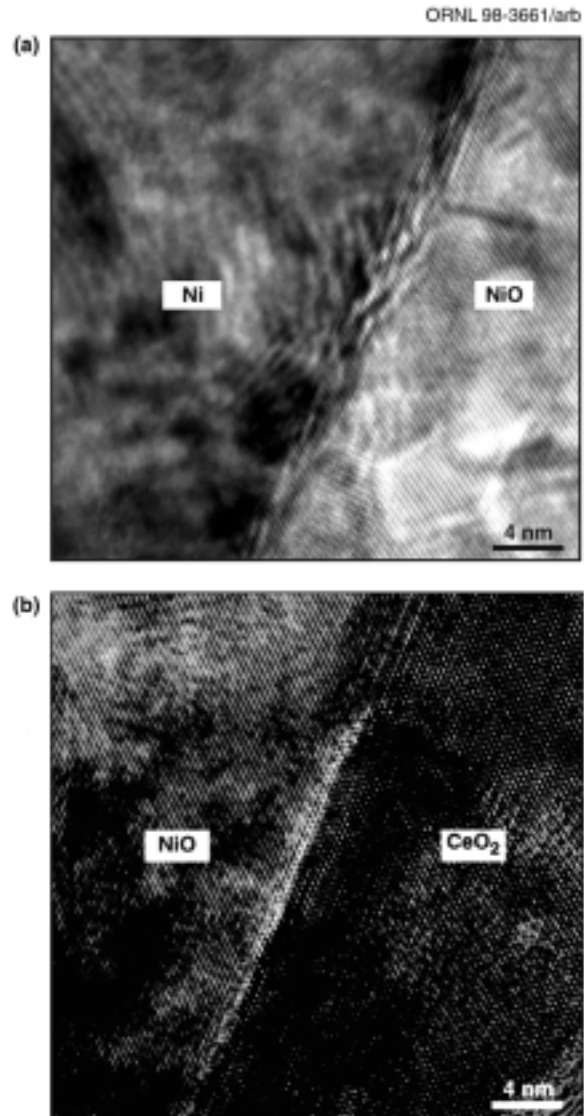
Ni/CeO_2 Interface

Interfacial reaction was found to occur at the Ni/CeO_2 interface, forming a 10–40-nm-

thick layer as shown in Fig. 1.45(*a*). This thin reaction layer had a cube-on-cube orientation with the Ni substrate, as revealed by both convergent beam diffraction patterns and high-resolution images. EDS analyses showed that Ni and O were the only elements detected in the interfacial layer [Fig. 1.45(*b*)]. Therefore, the reaction that occurred at the Ni/CeO$_2$ interface was oxidation of Ni. The interface between the reaction layer and the Ni substrate was atomically sharp [Fig. 1.46(*a*)]. However, the thickness of the oxide layer varied along the interface, and the NiO/Ni interface was concave in regions where the oxide was relatively thick, suggesting oxidation propagating from the

ORNL 98-3660/arb
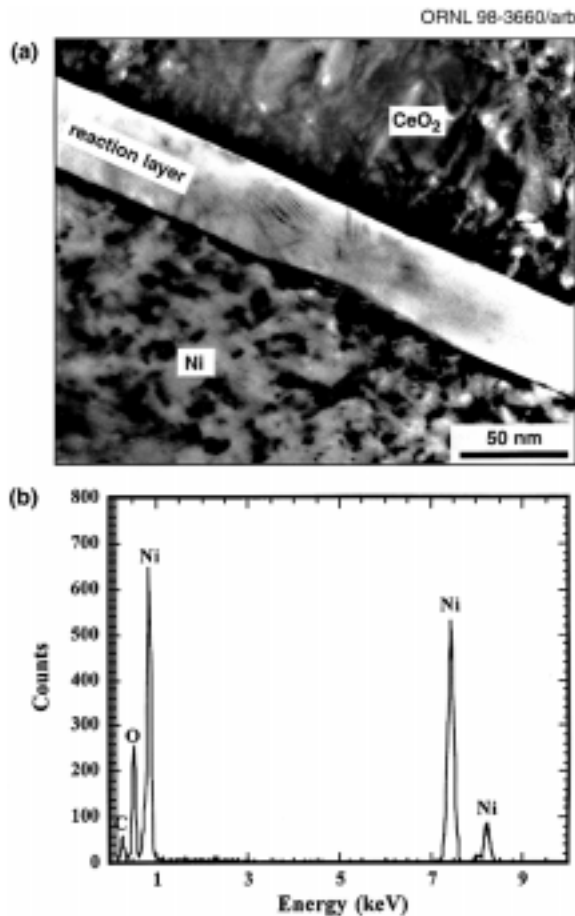
Fig. 1.45. (*a*) A reaction layer formed at the Ni/CeO$_2$ interface, and (*b*) EDS spectrum collected from the reaction layer.

ORNL 98-3661/arb

Fig. 1.46. High-resolution images of (*a*) the Ni/NiO interface and (*b*) the NiO/CeO$_2$ interface.

NiO/Ni interface into the Ni substrate. The interface between the NiO reaction layer and the CeO$_2$ buffer layer was sharp and flat, as shown in the high-resolution image in Fig. 1.46(*b*). A 45° in-plane rotation between the NiO layer and CeO$_2$ layer was observed. No interdiffusion of Ni and Ce across the interface between the reaction layer and the CeO$_2$ buffer layer was detected.

It is likely that the NiO layer formed after the initial epitaxy of CeO_2 on Ni because the initial deposition of CeO_2 was performed under oxygen partial pressures at which NiO is unstable. Formation of a Ni oxide layer at the Ni/CeO_2 interface after deposition of the initial CeO_2 layer could occur by solid-state oxygen diffusion through the CeO_2 layer and also by gaseous oxygen diffusion through the cracks in the CeO_2 layer, during the sequential deposition at high temperatures in an oxidizing environment. As mentioned earlier, after the initial deposition under reducing conditions, the CeO_2 film was deposited on the Ni tape at $780\,^\circ C$ under increasingly oxidizing conditions to eventually obtain stochiometric CeO_2. Furthermore, deposition of the YBCO layer was performed in a background O_2 pressure of 185 mtorr. These deposition conditions presented the possibility of oxygen diffusion to the Ni/CeO_2 interface. Previous studies have also shown that under certain deposition conditions, microcracks can form in the CeO_2 layer because of non-stoichiometry in the oxide layers, lattice mismatch stresses, and residual thermal expansion mismatch stresses between the CeO_2 layer and the Ni substrate. If microcracks form in the CeO_2 layer, diffusion of O_2 along the cracks can be expected, resulting in the preferential formation of NiO at the Ni/CeO_2 interface near the microcracking sites in the CeO_2 layer. This may explain the varying thickness of the NiO layer at the Ni/CeO_2 interface.

CeO_2 Layer

Three distinct morphologies were observed in the CeO_2 layer. As shown in Fig. 1.47(*a*), an equiaxed structure (A), ~25 nm thick, was formed during the initial deposition. The equiaxed structure was followed by an ~50-nm columnar structure (B) with the axis of the columns aligned along the [001] axis of CeO_2. The column spacing was ~20–25 nm. Following the columnar structure was again an equiaxial structure (C) through the rest of the layer. The
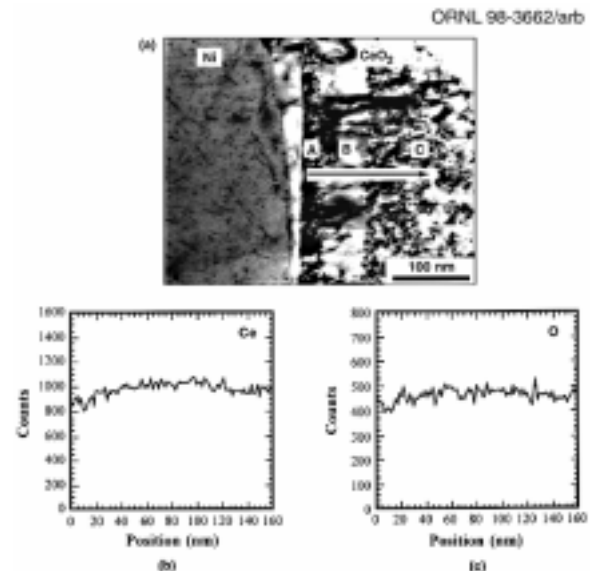
Fig. 1.47. (*a*) Three distinct morphologies observed in the CeO_2 layer: (A) an equiaxial structure, (B) a columnar structure, and (C) again an equiaxial structure through the rest of the layer; (*b*) Ce profile along the line-scan across the three different structures from A to C as indicated by the arrow in (*a*); and (*c*) O profiles collected along the line-scan across the three different structures from A to C as indicated by the arrow in (*a*).

first (A) and second (C) equiaxed structures were similar in appearance. Both contained very high dislocation densities. Conversely, the columnar structure (B) exhibited a very low dislocation density. Each individual column was essentially defect free. Detailed EDS analyses indicated that regions with different morphologies were of the same composition. Shown in Fig. 1.47(*b*) and (*c*) are Ce and O profiles recorded during a line scan across the three different structures as indicated in Fig. 1.47(*a*). No variation in either Ce or O concentration was detected.

The three distinct morphologies were found to correspond directly to the growth atmosphere during the deposition. The initial deposition of CeO_2 was performed in a forming gas containing H_2 in order to suppress oxidation of Ni. The estimated thickness of this initial layer was 10–30 nm, consistent with layer A observed

in TEM. After the initial deposition, the atmosphere was changed to an oxygen partial pressure of 10^{-5} torr. This change in atmosphere induced the columnar structure (B). The growth atmosphere was finally switched to an oxygen partial pressure of 4×10^{-4} torr, resulting in a change in the growth morphology back to equiaxed.

CeO₂ /YSZ Interface and YSZ Layer

The interface between the YSZ and CeO_2 layer was free of interfacial reactions, as shown in Fig. 1.48(*a*). Figure 1.48(*b*) is a high-resolution image showing lattice fringes extending across the interface. Composition analyses revealed that neither interdiffusion of elements nor interfacial reaction between the CeO_2 and the YSZ phases occurred. Periodic lattice distortions (dislocations) were present at the interface to accommodate the incommensurate lattice planes between the two phases as indicated by the arrow in Fig. 1.48(*b*). According to high-resolution XRD studies, the normally cubic CeO_2 and YSZ exhibited slightly distorted tetragonal structures due to the residual stresses: $a = b = 5.41$ Å and $c = 5.422$ Å for the CeO_2 and $a = b = 5.12$ Å and $c = 5.162$ Å for the YSZ. Therefore, the lattice mismatches in both a/b and c directions were 5.7% and 5.0%, respectively. The lattice mismatches corresponded to one dislocation site every ~20 lattice planes, consistent with the high-resolution image in Fig. 1.48(*b*).

The YSZ layer exhibited a columnar structure with a column spacing of ~40 nm [Fig. 1.48(*a*)]. The columns aligned along the [001] axis. High-resolution images revealed no orientation variation between the adjacent columns [Fig. 1.48(*b*)]. The contrast at the column boundaries was simply caused by dislocations originated from the CeO_2/YSZ interface.
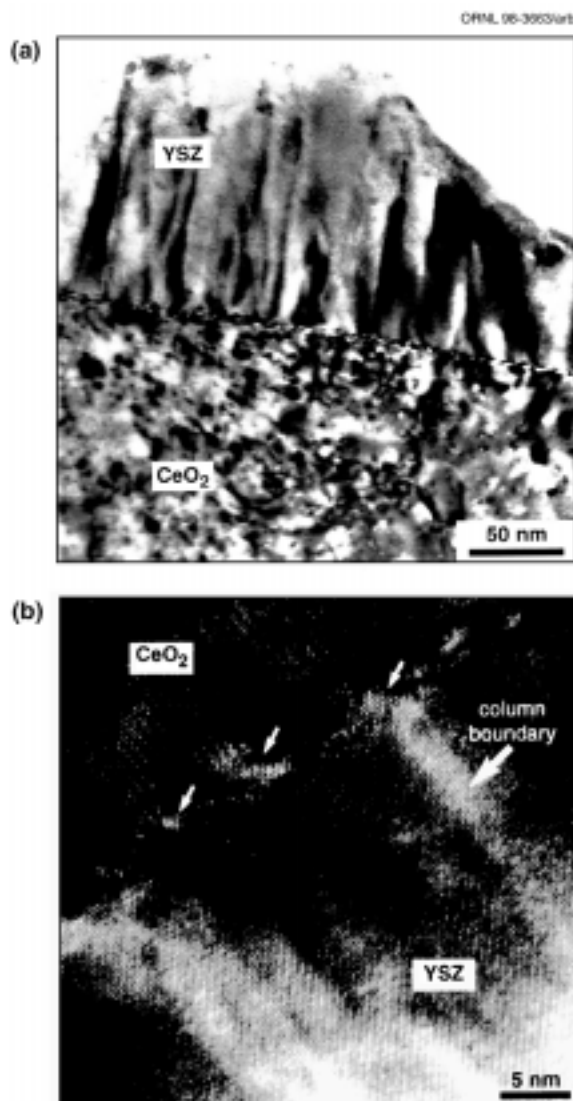
Fig. 1.48. (*a*) The interface between the CeO₂ and the YSZ layer and the columnar structure in the YSZ layer; and (*b*) a high-resolution image showing the periodic dislocations at the CeO₂/YSZ interface and revealing no orientation variation between adjacent columns in the YSZ.

Conclusions

The microstructure of a RABiTS™ comprised of epitaxial multilayers of YSZ (0.2 µm)/CeO_2 (0.9 µm) on a {100}<100> textured Ni (125 µm) template was determined using high-resolution electron microscopy. A reaction layer 10–40 nm thick was observed at the Ni/CeO_2 interface. Detailed microstructural and chemical analyses indicated that the layer was {001} nickel oxide on {001} Ni; however, the NiO layer was discontinuous, suggesting its formation after prior epitaxy of CeO_2 on Ni. Because only cube-on-cube orientation of NiO on Ni was observed, it may be possible to form a continuous layer of cube-oriented NiO by controlled oxidation of Ni as a suitable intermediate buffer layer. The CeO_2 layer was $45°$ in-plane rotated with respect to the Ni and NiO and was found to consist of three distinct morphologies corresponding to the growth conditions during the deposition. The multilayer studied is most susceptible to microcracking. Because there is a close correlation of the microstructure in the CeO_2 layer to the deposition conditions, it may be possible to control the morpology of this layer and hence alter the microcracking behavior. Columnar microstructures that in general are more resistant to crack propagation could be formed by performing the majority of CeO_2 deposition in a vacuum of 10^{-5} torr. Decreasing the thickness CeO_2 of the layer to below the critical thickness for cracking will also suppress microcrack formation. EDS compositional scans show negligible diffusion of Ni into the CeO_2 layer. Therefore, from the perspective of providing a diffusion barrier to YBCO, only tens of nanometers of CeO_2 are sufficient. Thin CeO_2 layers have been grown by e-beam evaporation of Ce metal on Ni. RABiTS™ with no microcracking in the CeO_2 layer exhibit J_cs approaching 3 MA/cm^2 at 77 K, 0 T. The YSZ layer exhibits a columnar structure aligned along the [100] axis, with little or no orientation variation between the columns. The interface between the YSZ and CeO_2 layer is atomically sharp and neither interdiffusion of elements nor an interfacial layer was observed. No evidence of microcracking in this layer was observed. Microstructral characteristics of the epitaxial YBCO layer will be reported elsewhere.